Comparative analysis of adhesive debonding in three-point bending tests using boundary element methods: Coupled criterion versus interface damage model

Sérgio Gustavo Ferreira Cordeiro, Thiago Birro, René Quispe Rodriguez, Eder Lima de Albuquerque, Lucas Silveira Campos, Jairo Francisco Useche Vivero, Éric Paroissien, Maëlenn Aufray, Frédéric Lachaud

Comparative analysis of adhesive debonding in three-point bending tests using boundary element methods: Coupled criterion versus interface damage model

Sérgio Gustavo Ferreira Cordeiro [a,*], Thiago V. Birro [b], René Quispe Rodriguez [c], Eder Lima de Albuquerque [d], Lucas Silveira Campos [e], Jairo Francisco Useche Vivero [f], Éric Paroissien [b], Maëlenn Aufray [g], Frédéric Lachaud [b]

[a] *Aeronautics Institute of Technology, Brazil*
[b] *Institut Clement Ader (ICA), Universite de Toulouse, ISAE-SUPAERO, INSA, IMT MINES ALBI, UTIII, CNRS, Toulouse, France*
[c] *Federal University of Santa Maria, Brazil*
[d] *University of Brasilia, Brazil*
[e] *Federal University of Espirito Santo, Brazil*
[f] *Universidad Tecnologica de Bolivar, Colombia*
[g] *CIRIMAT, Universite de Toulouse, CNRS, INP-ENSIACE, T 4 allee Emile Monso-BP44362, CEDEX 4, 31030 Toulouse, France*

MSC:
0000
1111

Keywords:
Adhesive joint design
Interface debonding
Boundary element method
Coupled criterion
traction-separation model

A B S T R A C T

Recent literature has introduced a novel quantitative approach for assessing critical stress and fracture toughness, utilizing a coupled stress energy criterion, commonly referred to as the coupled criterion (CC). However, evaluating the required parameters demands considerable effort using semi-analytical methods or finite element analysis techniques. The Boundary Element Method (BEM) provides an alternative to traditional approaches, as it eliminates the need for domain meshes and directly computes unknown field variables on the interfaces. The present study employs the CC and a 2D multi-zone BEM to access failure initiation and propagation in the adhesive interface of three-point bending test (3PBT's) with available experimental and numerical responses. The interface properties are then used in a progressive interface damage BEM analysis to evaluate the structural response of the tests and validate the values obtained for these properties. The study addressed both symmetric and asymmetric adhesive failure scenarios, indicating that the evaluation of fracture parameters in both cases is analogous because of the short crack length at the onset of failure. The results demonstrate that the use of the new quantitative methodology with BEM models, proposed herein, allows one to model complex geometries and interface debonding problems with greater accuracy and efficiency.

1. Introduction

Adhesively bonded joints have become increasingly popular in recent years due to their many advantages over traditional joining methods. Compared to welding, bolting, or riveting techniques, bonded joints offer more efficient load transfer, improved fatigue properties, improved corrosion resistance, smoother surfaces, and the possibility of conforming to lightweight structures [1,2]. Furthermore, with advances in adhesive science, adhesively bonded joints are stronger than ever, with higher peel and shear strengths and allowable ductility up to failure [3,4]. This makes them an attractive option for industries such as automotive and aviation, where reduced weight, uniform stress distribution, and the ability to join different materials are important considerations. Adhesive bonding is a versatile and effective technique for creating strong, durable, and lightweight joints.

Although adhesive bonding has proven to be a very promising technology, it is essential to evaluate its mechanical properties, such as load transfer capacity and toughness, to ensure safe and effective application. In terms of failure modes, adhesive failure, also known as adhesive-substrate failure or interface debonding, has been effectively avoided in the service life of bonded joints through industrial

* Corresponding author.
E-mail address: cordeiro@ita.br (S.G.F. Cordeiro).

https://doi.org/10.1016/j.enganabound.2025.106474

Nomenclature

α^2	Ratio of interfacial stiffness
$\bar{A}(S)$	Incremental energy function for a given position S along the overlap (N/mm^3)
β	Mixity ratio
Δa	Crack step (mm)
ΔS	Variation of crack area (mm^2)
δ	Norm of displacement jump (mm) of the interface
Δ_c	Global displacement discontinuity
δ_c	Critical displacement jump obtained using the Coupled Criterion (mm)
δ_e	Norm of displacement jump (mm) of the interface at the initiation of progressive damage law
δ_f	Norm of displacement jump (mm) of the interface at propagation of progressive damage law
δ_n	Opening displacement (mm)
δ_t	Slipping displacement (mm)
Γ^e	Boundary of element e
Γ_t	Neumann boundary
Γ_u	Dirichlet boundary
Γ_{c+}	Positive side of the interface
Γ_{c-}	Negative side of the interface
λ	Load factor
$\boldsymbol{\mathcal{R}}$	Residue vector
$\mathbf{e_i}$	Unit-length direction vector in direction i
$\mathbf{G}$	Dense square matrix from displacement kernel integration
$\mathbf{H}$	Dense square matrix from traction kernel integration
$\mathbf{k}$	Local initial stiffness matrix of the weak interface
$\mathbf{K}_c$	Interface stiffness matrix
$\mathbf{k}_c$	Global initial stiffness matrix of the weak interface
$\mathbf{R}$	Orthogonal transformation
$\mathbf{t}^\star(\mathbf{x}', \mathbf{x})$	Kelvin fundamental solutions for tractions
$\mathbf{T}$	Column matrix collecting traction coefficients $\mathbf{t}^e_\alpha$
$\mathbf{t}(\mathbf{x})$	displacement boundary field
$\mathbf{t}^e$	Traction approximation: $\mathbf{t}^e = N^e_\alpha \mathbf{t}^e_\alpha$
$\mathbf{t}^e_\alpha$	Traction coefficients
$\mathbf{T}_{c+}$	Traction on the positive side of the interface
$\mathbf{T}_{c-}$	Traction on the negative side of the interface
$\mathbf{u}^\star(\mathbf{x}', \mathbf{x})$	Kelvin fundamental solutions for displacements
$\mathbf{U}$	Column matrix collecting displacement coefficients $\mathbf{u}^e_\alpha$
$\mathbf{u}(\mathbf{x}')$	Displacement at the source point (mm)
$\mathbf{u}(\mathbf{x})$	Displacement boundary field
$\mathbf{u}^e$	Displacement approximation: $\mathbf{u}^e = N^e_\alpha \mathbf{u}^e_\alpha$
$\mathbf{u}^e_\alpha$	Displacement coefficients
$\mathbf{U}_{c+}$	Displacement on the positive side of the interface
$\mathbf{U}_{c-}$	Displacement on the negative side of the interface
$\mathbf{x}$	Vector of boundary field point coordinates mm
$\mathcal{C}\int$	Cauchy principal value integral
$\mathcal{G}$	Differential energy release rate (mJ mm^2 or N mm^{-1})
$\mathcal{G}^I_{dif}$	Component of incremental energy release rate (mJ mm^2 or N mm^{-1}) in mode I
$\mathcal{G}^I_c$	Critical energy release rate (mJ mm^2 or N mm^{-1}) in mode I
$\mathcal{G}^I_e$	Adhesive elastic energy stored (mJ mm^2 or N mm^{-1}) in mode I
$\mathcal{G}^{II}_c$	Critical energy release rate (mJ mm^2 or N mm^{-1}) in mode II
$\mathcal{G}^{II}_e$	Adhesive elastic energy stored (mJ mm^2 or N mm^{-1}) in mode II
$\mathcal{G}_c$	Fracture toughness (N mm^{-1})
$\mathcal{G}^{II}_{dif}$	Component of incremental energy release rate (mJ mm^2 or N mm^{-1}) in mode II
$\mathcal{G}_{inc}$	Incremental energy release rate (mJ mm^2 or N mm^{-1})
ν	Poisson's ratio
$\overline{\mathbf{T}}$	Nodal prescribed traction pattern
$\overline{\mathbf{U}}$	Nodal prescribed displacement pattern
ϕ	Phase angle of the displacement jump
ψ	Phase angle of the stresses jump
σ	Interfacial peel stress (MPa)
σ_c	Critical stress (MPa)
σ_{eq}	Equivalent stress (MPa)
τ	Interfacial shear stress (MPa)
$\mathbf{x}'$	Vector of boundary source point coordinates (mm)
$\vec{\delta}$	Vector of displacement discontinuities (mm)
$\vec{t}$	weak interface stress vector (MPa)
a	Crack length (mm)
$A(S)$	Differential energy function for a given position S along the overlap (N/mm^3)
a_c	Critical crack length (mm)
b	Overlap width (mm)
C	Compliance (mm/N)
D	Damage
d	Displacement of central roller (mm)
D_c	Maximum imposed displacement of central roller (mm)
E	Young's Modulus (MPa)
e	Boundary element
$f(\sigma_{ij}(x_i))$	Stress criterion (MPa)
$f_\mathcal{G}$	Normalized energy function
f_σ	Normalized stress function
F_c	Critical force in the three-point bending test (N)
h_a	Thickness of adhesive layer (mm)
h_s	Thickness of the substrate (mm)
$K(S)$	Stress function for a given position S along the overlap (MPa/mm)
K_{over}	Overall stiffness of the specimen (N mm^{-1})
K_{subs}	Overall stiffness of the substrate (N mm^{-1})
L	Length of bonded overlap (mm)
L_c	Characteristic fracture length of the interface

L_{mesh}	Mesh length (mm)
S	Crack area (mm^2)
S_c	Failure initiation area (mm^2)
t_c	Critical intant - failure initiation (s)
U	Prescribed displacement (mm)
W	Potential energy (mJ)
W_c	Dissipated energy (mJ)
W_k	Kinetic energy (mJ)
δ_{ne}	Displacement jump of the interface along the x-axis at the initiation (mm)
δ_{ne}	Displacement jump of the interface along the y-axis at the initiation (mm)
δ_{nf}	Displacement jump of the interface along the y-axis at the propagation (mm)
δ_{tf}	Displacement jump of the interface along the x-axis at the propagation (mm)
σ_{nc}	Critical peel stress (MPa)
τ_{tc}	Critical shear stress (MPa)
k_{n0}	Interfacial stiffness (MPa mm^{-1}) under mode I
k_{t0}	Interfacial stiffness (MPa mm^{-1}) under mode II
3PBT	Three-Point Bending Test
BEM	Boundary Element Method
BIE	Boundary Integral Equation
CC	Coupled Energy Stress Criterion
DETA	Diethylenetriamine
DGEBA	Polyepoxide bisphenol A diglycidyl ether
EB	Euler–Bernoulli
ERR	Energy Release Rate
FEM	Finite Element Method
FFM	Finite Fracture Mechanics
LEBIM	Linear Elastic-(Perfectly) Brittle Interface Model
LEFM	Linear Elastic Fracture Mechanics
LEP	Linear Elastic Propagation
ME	Macro-element
PID	Progressive interface damage
SGBEM	Symmetric Galerkin BEM
TSM	Traction-Separation Models

practices. Adhesive failure is, in fact, one of the key criteria for rejecting an adhesive bonding system, often prompting modifications to the adhesive, substrates, or manufacturing process to prevent it. Unfortunately, adhesive failure remains difficult to understand and predict. Adhesive-bonded joints have been found to exhibit unstable behavior and there is a lack of comprehensive understanding of adhesive failures, particularly in critical systems. The main reason for this is the complexity of the interactions between the adhesive and the bond surface, which require consideration of many factors based on theoretical and experimental techniques developed over the years. Therefore, a comprehensive multidisciplinary approach is necessary to understand these interactions [5].

Mittal (1978) [6] suggests that relying solely on the failure mode as a criterion to evaluate bonded joints is insufficient. In some cases, joints that fail due to adhesive failure can demonstrate greater strength than those that fail cohesively. As a result, the ultimate strength of the joint should be the primary criterion for approving adhesively bonded joints, as long as the failure mode and the corresponding load can be accurately predicted. This underscores the importance of modeling adhesively bonded joints as a critical step in the evaluation process.

2. Modeling adhesively bonded joints and failure prediction

In the framework of interface modeling, two approaches can be used to model the interface between different materials: weak interface modeling and strong interface modeling [7]. In strong interface modeling, it is assumed that there is a perfect bond between dissimilar materials, as shown in Fig. 1.a. This approach typically leads to stress singularities and an oscillatory character [8–10]. On the other hand, weak interface modeling uses a continuous distribution of linear springs [7] that couple the kinematics of the bonding surfaces. Weak interface modeling is typically associated with a thin adhesive layer (only if homogeneous stress can be assumed through the layer), fiber-matrix interfaces [11] or bonded interfaces [12], as shown in Fig. 1.b. This approach results in displacement discontinuities, but assumes continuous tractions. According to Cornetti et al. (2012) [7], weak interface modeling can be used as an initial approximation of the actual adhesive behavior.

Interface modeling has been recognized for quite some time, yet solely relying on it is insufficient for predicting failure without the integration of specific failure criteria, thus emphasizing its significance as a research area. In their review of the failure of elastic interfaces, Cornetti et al. (2006) [13] shed light on the limitations of Linear Elastic Fracture Mechanics (LEFM). Although LEFM is a valuable tool for studying crack growth, it falls short in one crucial aspect: it can only predict the propagation of an existing crack, leaving the initiation of a new one uncharted. The coupled energy stress criterion (CC) can be used to overcome this limitation [14]. The CC assumes that a finite-size crack forms instantaneously at the beginning of failure. Both energy and stress criteria are required for fracture, but neither is enough on its own. CC has successfully solved various fracture mechanics problems, such as crack initiation in a four-point bending test [15], single-lap joint [16], or in the pull-push shear test [17]. Experimental data have been used in a blind analysis (or inverse analysis), in which failure loads and crack lengths are measured or estimated to assess the fracture properties of the interface [18,19].

Another classical method to predict adhesive failure (initiation and propagation) is based on traction-separation models (TSM) prior to the final opening of the crack. Initially, the singularity near the tip of the crack is removed by assuming cohesive forces that hold the opposite surfaces [20]. In 1994, Tvergaard [21] applied a similar approach to predict the initiation and spread of damage at an interface using TSM. Since then, several works have used TSM to investigate adhesive failure problems [22–24]. The main advantages of TSM for the analysis of adhesive failure are: (i) They allow the modeling of interface failure initiation, and (ii) they allow the modeling of adhesive joints from brittle to ductile failure behaviors. However, they required the solution of nonlinear problems, and, therefore, they are more computationally demanding.

Interface modeling entails simplifying physical reality through a set of assumptions which are then expressed as mathematical equations that need to be solved. An analytical solution, expressed as a closed-form equation, might be achievable if the underlying assumptions are sufficiently robust. However, if assumptions diverge excessively from reality, the results may differ significantly from the experimental data. In situations where an analytical solution is impractical due to more flexible assumptions, a semi-analytical method utilizing numerical techniques with specialized software can be employed. When an accurate representation of real-world conditions through assumptions becomes challenging, engineers often employ advanced numerical methods to solve complex models. In the context of adhesively bonded joint analysis, the Finite Element Method (FEM) has been extensively utilized, originally developed to address limitations inherent in analytical techniques, such as the omission of adhesive thickness or the assumption of uniform stress distribution. Over time, FEM has been refined and expanded to address a broader range of applications, including the

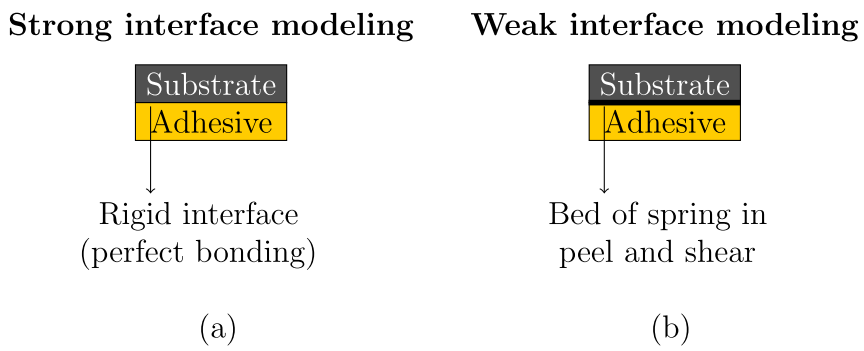

Fig. 1. Interface modeling: (a) Strong interface modeling, where a rigid interface is adopted (perfect bonding), and (b) weak interface modeling, where a bed of springs in peel and shear is adopted.

modeling of nonlinearity of the material, shape optimization, contributions of joint stiffness to structural behavior, and characterization of stress fields near singularities. However, analytical solutions consistently demonstrate the presence of steep stress gradients at the edges of the bonded joints, requiring significant efforts in mesh refinement and convergence within FEM to achieve the necessary level of precision.

In this regard, the Boundary Element Method (BEM) presents a viable alternative, particularly in cases where stress gradients and joint parameters are critical to the analysis. Unlike FEM, which discretizes the entire domain of the structure, BEM discretizes only the boundary, making it highly efficient for problems involving stress concentrations and singularities, such as those encountered at the interface corners of bonded joints. Moreover, BEM offers advantages in handling complex geometries with fewer elements compared to FEM, thus simplifying the modeling of joints where adhesive thickness and geometric features significantly influence the stress distribution. Therefore, BEM serves as a complementary numerical tool to FEM, providing distinct advantages for specific classes of problems, particularly in the accurate representation of stress gradients, without being inherently superior or inferior to FEM [25].

To the best of the author's knowledge, only a very limited number of studies exist on the application of the CC and BEM to adhesively bonded joints [17] or focusing specifically on the use of the CC to predict adhesive failure [26]. Both works share only one common point: the use of a model known as the Linear Elastic-(Perfectly) Brittle Interface Model (LEBIM). In this model, three mechanical properties of the interface are directly coupled: fracture toughness, strength, and interface stiffness. Therefore, when two of these properties are known, the third can be directly calculated. However, Muñoz-Reja highlighted a limitation of this model: as the interface becomes stiffer, LEBIM may produce inaccurate predictions. This issue is attributed to the highly restrictive coupling between some of the model parameters (fracture toughness, strength, and interface stiffness).

On the other hand, there are several works devoted to incorporating TSM in BEM, as deeply addressed by [27]. In the frame of interface debonding and TSM law, a few works can be mentioned, such as a problem involving the debonding of fiber reinforced polymer bonded over a concrete element that was studied by Tin-Loi and Li (2000) [28], a quasi-static model for crack-mode-sensitive interface damage with linearly elastic bodies at small strains using Symmetric Galerkin BEM (SGBEM) [29], the prediction of interface damage using SGBEM models of a double cantilever beam test [30] and a quasi-static delamination model with rate dependence under cyclic loading [31]. Traditionally, FEM has been the method of choice for such analyses. For example, Wang et al. (2023) [22] modeled the failure of ductile adhesives using the trapezoidal mixed-mode cohesive zone model implemented in Abaqus. Similarly, Xu et al. (2017) [23] investigated the impact of different cohesive laws on the simulation of adhesive failures in composite structures using an improved interpolation-based cohesive zone model. Furthermore, Gheibi et al. (2023) [24] developed a cohesive zone model based on the Park–Paulino–Roesler model to predict the behavior of ductile adhesives, especially under mixed-mode loading. However, the analysis of problems which require accurate interface stresses field evaluation, such as adhesive debonding analysis, can be quite challenging to perform using classical FEM because of the very fine meshes required at the adhesive interfaces, which spread over the domain due to domain discretization requirements. On the other hand, the BEM presents an interesting alternative for such problems, because it naturally approximates the interface stresses with great accuracy. BEM is devoted to solving the problem by first rewriting it in terms of Boundary Integral Equations (BIE) and then by directly calculating the unknown displacement and traction field variables on the boundary and interfaces without requiring a domain discretization. In addition, BEM offers several facilities to generate geometrically complex analysis models due to the absence of the requirement of domain discretization [32].

In contrast to finite element approaches, this work uses CC with weak interface 2D multi-zone BEM models in plane stress to access, through an inverse analysis, the critical stress and fracture toughness of the adhesive bonding interface in a three-point bending (3PBT) test with available experimental, semi-analytical, and numerical responses. An intrinsic mixed mode TSM is then employed to simulate the structural response of the tests by incorporating the accessed properties of the bonding interface into local interfacial stiffness matrices of the boundary element equations. To the best of the authors' knowledge, this novel approach has not been previously documented in the literature. The results demonstrate that the boundary element method is highly suitable for this type of problem, providing models to quantify the properties of the bonding adhesive interface and to perform adhesive debonding analysis with a reduced number of degrees of freedom that are both accurate and user-friendly.

3. The three-point bending test

The 3PBT introduced by Roche et al. (1982) [33] involves an epoxy-based adhesive bonded directly to a substrate sheet. The test specimen can be arranged in two different ways: a substrate-coating-adhesive or a substrate-adhesive system. Despite the fact that coated and uncoated specimens have similar fracture mechanisms, both configurations focus only on one interface, providing a remarkable failure initiation zone [34,35].

3.1. Test protocol

Fig. 2 illustrates the substrate-adhesive system, in which the substrate is bonded to a stiff adhesive block. A central displacement is imposed on the specimen, which causes a stress concentration near the corner where the adhesive and the substrate meet. As a result, adhesive failure occurs. The dimensions, the reference planes, and specifications

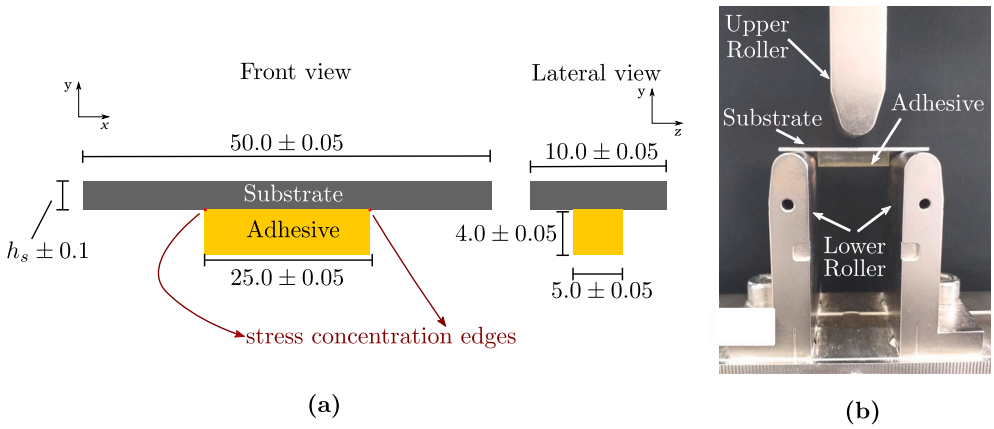

Fig. 2. (a) Dimensions (in mm) following the ISO standard 14679-1997 [36] (b) Experimental setup of the 3PBT.

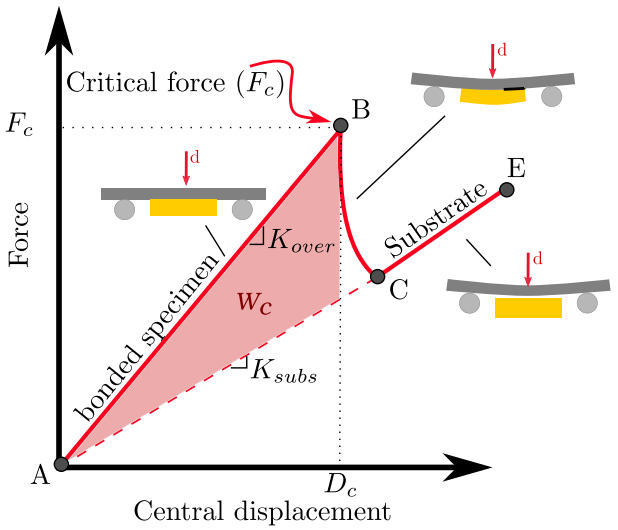

Fig. 3. Typical response of the 3PBT: AB – specimen stiffness; B – instantaneous failure initiation; BC – Failure propagation; CE – substrate stiffness.

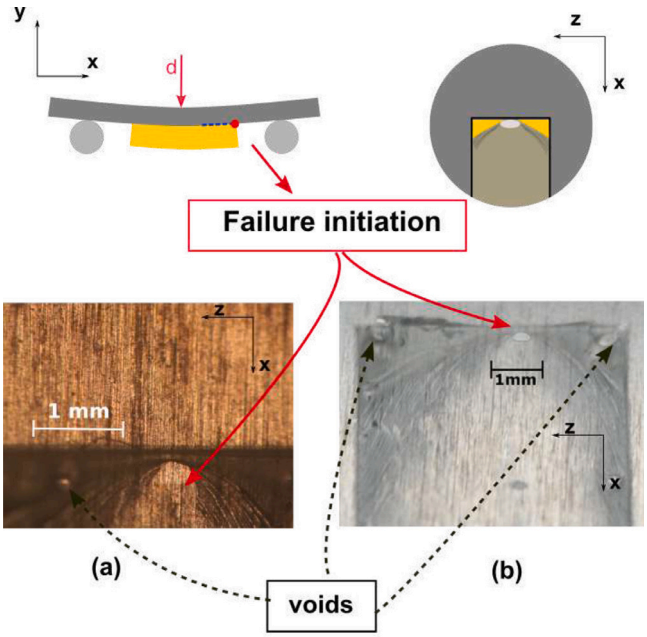

Fig. 4. Images from the initiation of interface debonding (post-mortem): (a) Optical micrograph using artificial lights and (b) high-definition camera using sunlight.

shown in Fig. 2 comply with the ISO standard 14679-1997 [36], where h_s represents the thickness of the substrate.

A typical structural response curve of the test is shown in Fig. 3. It can be seen that the force increases until a critical value (F_c) is reached (AB), and the failure is initiated. The force drops suddenly due to adhesive failure (BC). At the end of the test, the force increases again, but now only the substrate stiffness is left (CE). It should be noted that F_c is directly dependent on the thickness of the substrate. If the substrate is thicker, F_c will be greater. The area between the lines AB, AC, and BC corresponds to the energy that is dissipated (W_c). The stiffness of the bonded specimen and the stiffness of the substrate are indicated as K_{over} and K_{subs}, respectively.

The test can provide a measurable area associated with the initiation of failure, which is illustrated in Fig. 4. Devos et al. (2001) [37] used acoustic emission to evaluate the failure initiation of 3PBT. The analysis revealed that micro-cracks appeared before a critical crack length could be seen on the mesoscale. The point B in Fig. 3 corresponds to the exact moment when the length of the micro-cracks exceeds a critical crack length (a_c), leading to a loss of overall stiffness. This exact point is considered as the start of the failure (point B) and is assumed to correspond to the visible crack surface in a postmortem analysis (see Fig. 4) [34,35].

Regarding the post-morten analysis and measurement of the failure initiation surface, two different optical systems were available to assess the failure initiation zone: The high definition camera (Nikon D3) and the optical microscope (Wild Makroscop M420). Hence, a representative case of adhesive failure initiation was measured for both methods, as demonstrated in the post-mortem analysis shown in Fig. 4. Even if some bubbles may eventually appear only in the bulk adhesive, a central round area is indicated in Fig. 4.

The initiation areas (as shown in Fig. 4-a and -b) were calculated using ImageJ, an open-source image processing software. The measurement of small round areas following both techniques is reported for both substrate thicknesses in Table 1. It is shown that (i) the measurements of both techniques are in close agreement and (ii) the standard deviations are low.

In the experimental campaign, crack initiation and propagation were observed to be asymmetrical, with approximately the same 50% probability of occurring on either side of the adhesive layer. Regarding the stability of crack propagation, the experimental results demonstrated a predominantly brittle and unstable fracture process. The crack

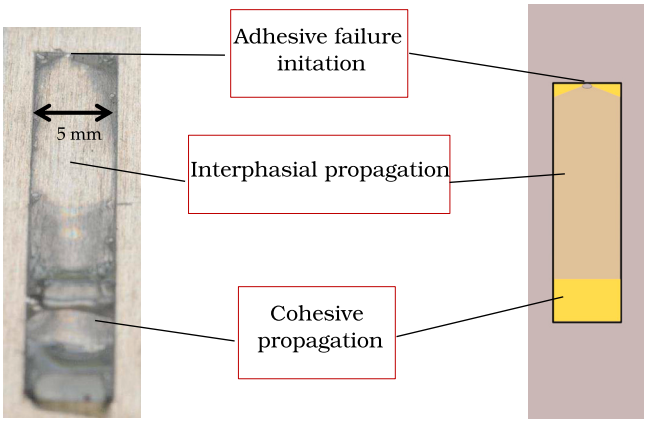

Fig. 5. Typical fracture behavior in a post-mortem analysis: from failure initiation to propagation.

Table 1
Experimental results from the analyzed substrate-adhesive systems.

Substrate thickness	F_c (N)	K_{over} (N mm^{-1})	S_c (mm^2)
1.08 mm	178 ± 26	309 ± 9	0.102 ± 0.02
1.62 mm	326 ± 50	535 ± 13	0.07 ± 0.01

Table 2
Mechanical properties of adhesive and substrate - Sauvage et al (2017) [34].

	E (MPa)	ν
DGEBA/DETA/Organosilane	3000	0.35
Aluminium 2024-T3	68 000	0.33

front progressed along the bonded overlap and, when it reached the end of the adhesive interface, continued to propagate into the bulk polymer, as shown in Fig. 5.

3.2. Case of studies

In the present work, two similar substrate-adhesive systems with different geometries are studied. In preparing the three-point bending specimens, an aluminum alloy 2024-T3 substrate, sourced from Rocholl GmbH, was used in two thicknesses: 1.08 and 1.62 mm. The adhesive consisted of a polyepoxide bisphenol A diglycidyl ether (DGEBA) with functionality 2, provided by Dow Chemical, and a diethylenetriamine (DETA) hardener with functionality 5. Furthermore, organosilane GLYMO (3-Glycidyloxypropyl) trimethoxysilane, with functionality 1, supplied by Sigma-Aldrich, was included as an adhesion promoter, which constitutes 5% by weight of the resin. The substrate preparation involved degreasing with acetone, followed by etching with nitric acid. The samples were immersed in a 6.3 mol/L nitric acid solution at 50 °C for 10 min. After etching, the samples were rinsed with deionized water and dried at room temperature. This acid etching process created a new passivation layer and removed impurity particles.

The experimental parameters required for the study of the two systems are listed in Table 1. It should be emphasized that the authors did not use the displacement at the onset of crack propagation, provided by the bending machine, due to the initial gap between the roller and the specimen. Instead, the values of K_{over} and F_c are used to calculate the critical displacement, which is calculated as $D_c = F_c/K_{over}$.

The analyzes also require the mechanical characteristics of the adhesive and substrate, which are assumed to display linear elastic behaviors. Sauvage (2017) et al. [34] identified the elastic properties of both materials, and their values are shown in Table 2.

Table 3
Interfacial stiffness in peel and shear for different h_s values.

h_s (mm)	k_{n0} (MPa/mm)	k_{t0} (MPa/mm)
1.08	2000	2000
1.62	948	948

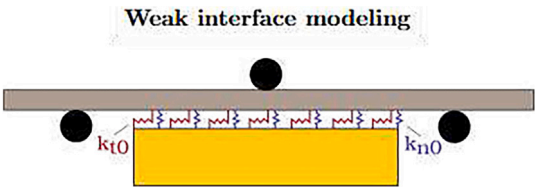

Fig. 6. Representation of a bed of springs in peel and in shear to couple the kinematics of the substrate and the adhesive.

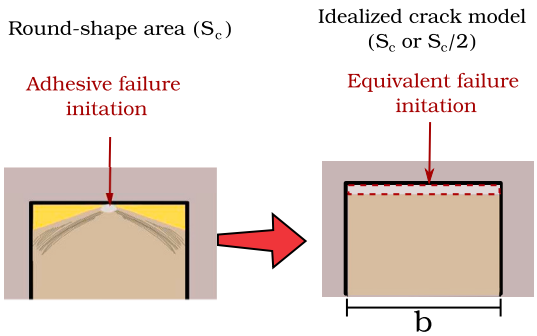

Fig. 7. Equivalent fracture length model.

The initial stiffness of the weak interface in mode I (k_{n0}) and mode II (k_{t0}) are assumed to be the same as used by Birro et al. (2020) [35], who calibrated these values using a numerical model to match the experimentally obtained K_{over} values. Birro et al. (2020) [35] stated that there are numerous combinations available to satisfy this condition, and a no mode-differentiation ($k_{n0} = k_{t0}$) assumption was made based on similar studies in the literature [15,38]. This approach yielded satisfactory results in terms of predicting load initiation. The interfacial stiffness obtained for both substrate configurations are listed in Table 3.

4. Adhesive failure approach

4.1. Weak interface modeling

In the present work, only weak interface modeling is considered hereafter, as shown in Fig. 6. In this case, the normal and tangential interfacial stresses σ and τ relate to the normal and tangential relative displacements δ_n and δ_t before interface failure by linear relations: $\sigma = k_{n0}\delta_n$ and $\tau = k_{t0}\delta_t$, where k_{n0} and k_{t0} are the initial stiffness of the weak interfaces in mode I and mode II, respectively (see Table 3).

In the following, both the CC and the progressive damage interface modeling based on cohesive traction-separation laws are discussed and formulated to predict adhesive failure in the framework of weak interface modeling for the 3PBT.

As shown in Fig. 4, adhesive failure initiation typically occurs as a circular zone. However, due to limitations inherent to 2D numerical modeling, such rounded geometries could not be accurately represented. To address this, an idealized crack was introduced, modeled as a narrow strip that covered the entire width of the specimen, as illustrated in Fig. 7. This idealization allowed an equivalent representation of the physical behavior observed experimentally in a 2D model.

4.2. Finite fracture mechanics

In finite fracture mechanics (FFM), the instant of the initiation of a crack under quasi-static loading conditions requires that two criteria are met together, known as the coupled stress and energy criterion or CC [14].

4.2.1. Stress criterion

The first criterion is that the stress state must be high enough throughout the expected crack path before crack nucleation can occur. This criterion states that every point x_i along the expected crack path Γ_c should fulfill the stress criterion $f(\sigma_{ij}(x_i))$. This approach is called a point-wise formulation and can be expressed as follows:

$$f(\sigma_{ij}(x_i)) \geq \sigma_c \ \forall \ x_i \in \Gamma_c. \tag{1}$$

In the present work, an equivalent stress criterion based on the equivalent relative displacement of the interface is adopted. From the relative displacements δ_n and δ_t, the displacement discontinuity vector is defined as $\vec{\delta} = \left\{\delta_n,\ \delta_t\right\}^{\mathrm{T}}$. Its Euclidean norm $\|\vec{\delta}\|$, also called the equivalent relative displacement, is

$$\|\vec{\delta}\| = \delta = \sqrt{\delta_n^2 + \delta_t^2}. \tag{2}$$

If k_{n0} and k_{t0} take different values, then $\vec{\delta} = \left\{\delta_n,\ \delta_t\right\}^{\mathrm{T}}$ and the stress vector of the interface $\vec{t} = \{\sigma,\ \tau\}^{\mathrm{T}}$ are not collinear vectors. Then two phase angles ϕ and ψ are defined as well as a mode mixity ratio β:

$$\begin{cases} \beta = \tan(\phi) = \delta_t/\delta_n, \\ \tan(\psi) = \tau/\sigma. \end{cases} \tag{3}$$

The phase angles are linked as follows:

$$\tan(\psi) = \frac{\tau}{\sigma} = \frac{k_{t0}\delta_t}{k_{n0}\delta_n} = \frac{k_{t0}}{k_{n0}}\tan(\phi) = \alpha^2\beta, \tag{4}$$

where $\alpha^2 = k_{t0}/k_{n0}$. The notation σ_{eq} is used instead of $f(\sigma_{ij}(x_i))$ to denote the equivalent stress. The equivalent stress adopted in the stress criterion is linearly dependent on the equivalent displacement through a stiffness function k of β (or ϕ), as follows:

$$\|\vec{t}\| = \sigma_{eq} = \sqrt{\sigma^2 + \tau^2} = \sqrt{1 + \left(\alpha^2\beta\right)^2}\sigma \tag{5}$$

or

$$\sigma_{eq} = \sqrt{1 + \left(\alpha^2\beta\right)^2}k_{n0}\cos(\phi)\delta = k_{n0}\frac{\sqrt{1 + \left(\alpha^2\beta\right)^2}}{\sqrt{1+\beta^2}}\delta = k(\beta)\delta, \tag{6}$$

where

$$k(\beta) = k_{n0}\frac{\sqrt{1 + \left(\alpha^2\beta\right)^2}}{\sqrt{1+\beta^2}} = k_{n0}\sqrt{\cos^2(\phi) + \alpha^4\sin^2(\phi)}. \tag{7}$$

The relative displacements of the interface δ_n and δ_t, as well as the interfacial stresses σ and τ can be obtained from the projection of the vectors $\vec{\delta}$ and $\vec{t}$, leading to:

$$\begin{cases} \delta_n = \cos(\phi)\delta = \frac{1}{\sqrt{1+\tan^2(\phi)}}\delta = \frac{1}{\sqrt{1+\beta^2}}\delta = \frac{1}{k(\beta)\sqrt{1+\beta^2}}\sigma_{eq}, \\ \delta_t = \sin(\phi)\delta = \frac{\tan(\phi)}{\sqrt{1+\tan^2(\phi)}}\delta = \frac{\beta}{\sqrt{1+\beta^2}}\delta = \frac{\beta}{k(\beta)\sqrt{1+\beta^2}}\sigma_{eq}, \\ \sigma = \cos(\psi)\sigma_{eq} = \frac{1}{\sqrt{1+\tan^2(\psi)}}\sigma_{eq} = \frac{1}{\sqrt{1+\left(\alpha^2\beta\right)^2}}\sigma_{eq}, \\ \tau = \sin(\psi)\sigma_{eq} = \frac{\tan(\psi)}{\sqrt{1+\tan^2(\psi)}}\sigma_{eq} = \frac{\alpha^2\beta}{\sqrt{1+\left(\alpha^2\beta\right)^2}}\sigma_{eq}. \end{cases} \tag{8}$$

When the equivalent stress reaches the critical tensile stress $\sigma_{eq}(\beta_c) = \sigma_c$, a particular mixed-mode ratio β_c is identified. The equivalent relative displacement δ_c is also identified and reads $\delta_c = \sigma_c(\beta_c)/k(\beta_c)$. When the critical relative displacement δ_c and the critical relative stress σ_c are known, Eq. (8) provides, as a function of β_c, the relative displacements and interfacial stresses in pure modes reached at the beginning of crack propagation: $\delta_n(\delta_c)$, $\delta_t(\delta_c)$, $\sigma(\sigma_c)$, $\tau(\sigma_c)$. It is emphasized that these values are not the critical ones at the beginning of propagation in pure modes, which are termed: δ_{nc}, δ_{tc}, σ_{nc}, τ_{tc}.

4.2.2. Energy criterion

The second criterion that must be reached to initiate the formation of a crack involves the balance between the potential energy (W), the kinetic energy (W_k), and the energy $\mathcal{G}_c(\Delta S)$ required for the formation of a finite crack area ΔS. When dealing with quasi-static conditions, the production of kinetic energy can be ignored ($\Delta W_k = 0$). To ensure that the incremental energy release rate (ERR) under quasi-static conditions, i.e. $\mathcal{G}_{inc} = \Delta W_p/\Delta S$, is consistently defined, it must satisfy

$$\mathcal{G}_{inc}(S) = \frac{W(0) - W(S)}{\Delta S} \geq \mathcal{G}_c, \tag{9}$$

where $\mathcal{G}_c$ is the critical ERR.

For a two-dimensional model, it is assumed that the fracture area (ΔS) occurs throughout the width b of the model, thus $\Delta S = b \cdot a$, where a is the length of the crack. As explained by Weißgraeber et al. (2016) [39], the incremental ERR $\mathcal{G}_{inc}$ corresponds to the average of the differential ERR $\mathcal{G}$.

$$\mathcal{G}_{inc} = \frac{1}{\Delta a}\int_0^{\Delta a}\mathcal{G}(a)\mathrm{d}a \quad \text{or} \quad \frac{\mathrm{d}\mathcal{G}_{inc}}{\mathrm{d}a}\Delta a + \mathcal{G}_{inc} = \mathcal{G}. \tag{10}$$

4.2.3. The coupled energy-stress criterion

The notion of linear elastic materials under the assumption of small deformation theory considerably simplifies the statement of the CC. In this case, the equivalent stress σ_{eq} is directly proportional to the applied load or displacement. Furthermore, the potential energy of the cracked and uncracked interface is proportional to the square of the applied load or displacement [40]. These relations can be written as follows:

$$\begin{cases} \sigma_{\mathrm{eq}}(S) = K(S)U = \sigma_c, \\ \mathcal{G}_{inc}(S) = \bar{A}(S)U^2 = \mathcal{G}_c, \end{cases} \tag{11}$$

where $K(S)$ and $\bar{A}(S)$ are problem-dependent functions of crack size S and U is the prescribed displacement value (the prescribed vertical displacement in the case of the 3PBT). In addition, the coefficient $K(S)$ can be computed by a single linear elastic analysis of the problem with a weak, noncracked interface and a unit-imposed displacement U. On the other hand, the computation of $\bar{A}(S)$ requires several linear elastic analyzes with increasing crack area sizes S. Note that $K(S)$ and $\bar{A}(S)$ are independent of the tensile strength of the material and the critical ERR. Assuming f_σ and $f_\mathcal{G}$ as follows:

$$\begin{cases} f_\sigma = \sigma_{\mathrm{eq}}(S)/\sigma_c, \\ f_\mathcal{G} = \mathcal{G}_{inc}(S)/\mathcal{G}_c. \end{cases} \tag{12}$$

Under these assumptions, the CC is fulfilled when

$$f_\sigma(S) \geq 1 \quad \wedge \quad f_\mathcal{G}(S) \geq 1, \quad \forall\ S \in \Gamma_c. \tag{13}$$

Remark 1. The CC presented in Eq. (13) is used when the fracture properties $\mathcal{G}_c$ and σ_c are known. Conversely, it is also possible to use an inverse approach to compute those fracture properties with the energy and the stress criterion in Eq. (11) if the critical displacement $U = D_c$ and the crack area S_c are known. The inverse approach is adopted herein to determine the interface fracture properties of the analyzed substrate-adhesive systems.

4.3. Crack propagation

Once crack initiation is determined, crack propagation based on linear elastic fracture mechanics can be analyzed using Griffith theory [41], as follows:

$$\mathcal{G}(S) = \frac{dW}{dS} \geq \mathcal{G}_c. \tag{14}$$

Following [42], the relationship between the incremental ERR of the FFM and the differential ERR from Griffth's theory is given by:

$$\mathcal{G}_{inc}(S) = \frac{1}{S}\int_0^S \mathcal{G}(\xi)\,\mathrm{d}\xi. \tag{15}$$

As demonstrated by Martin et al. (2016) [15], FFM can be relied upon Griffth's theory. Notice that the known function $\bar{A}(S)$ can be presented as:

$$\bar{A}(S) = \frac{1}{S}\int_0^S A(\xi)\,\mathrm{d}\xi, \tag{16}$$

where, analogously to the energy criterion in Eq. (11), A can be expressed depending on the differential ERR $\mathcal{G}(S)$ as follows:

$$A(S) = \frac{G}{U^2}. \tag{17}$$

For a constant prescribed displacement, the crack growth occurs when:

$$A(S) = \frac{\mathcal{G}}{U^2} \geq \frac{\mathcal{G}_c}{U^2}. \tag{18}$$

The fracture energy $\mathcal{G}$ can be obtained from linear beam theory using the classic Irwin-Kies expression for the fracture energy for applied displacement [43], resulting in the following:

$$\mathcal{G} = \frac{U^2}{2C^2}\frac{\mathrm{d}C}{\mathrm{d}S}. \tag{19}$$

where $C = U/F(U)$, with $F(U)$ being the central load corresponding to a displacement U. Substituting Eq. (19) into Eq. (18), the following propagation criterion is obtained:

$$\frac{1}{2C^2}\frac{\mathrm{d}C}{\mathrm{d}S} \geq \frac{G_c}{U^2}, \tag{20}$$

which can be rewritten as:

$$U \geq C\sqrt{\frac{2\mathcal{G}_c}{\mathrm{d}C/\mathrm{d}S}}. \tag{21}$$

Remark 2. In the 3PBT under study, a constant velocity is imposed in the middle of the sample. As a consequence, the displacement must have a monotonic increase, which means that equation $U(t_c+\Delta t) > U(t_c)$ needs to be satisfied, where t_c corresponds to the instant the failure starts. Therefore, the propagation criterion in Eq. (21) is rewritten as follows:

$$U(t_c + \Delta t) \geq \max\left(C\sqrt{\frac{2\mathcal{G}_c}{\mathrm{d}C/\mathrm{d}S}}, U(t_c)\right). \tag{22}$$

4.4. Progressive interface damage modeling

Cohesive traction-separation laws can be an interesting approach to model progressive interface damage (PID). The region ahead of the crack tip along the interface in which the damage occurs is called the fracture process zone. The traction-separation laws provide a constitutive relation between the stresses at the damage interface $\vec{t}$ and the displacement discontinuities $\vec{\delta}$ along the process zone. Several traction-separation laws are available in the literature [44]. The bilinear traction-separation relationship from [45], which is completely characterized by the CC parameters, is an interesting alternative to simulate adhesive failure and is adopted in the present work.

The classical displacement-control method is used to perform the nonlinear progressive damage analysis and assess the interface damage in the process zone. The idea in this section is to present a simplified displacement-control approach without fracture mode differentiation, in which the parameters $\mathcal{G}_c$ and σ_c of the couple criterion can be used directly. The interface traction-separation law is assumed to have a classical bilinear form. To introduce the model, the definitions of the equivalent relative displacement δ and the mixity parameter β are recalled.

$$\delta = \|\vec{\delta}\| = \sqrt{\delta_n^2 + \delta_t^2} \quad \text{and} \quad \beta = \tan(\phi) = \frac{\delta_t}{\delta_n}. \tag{23}$$

For a given load step of the nonlinear progressive damage analysis, the mixity parameter β is updated at each iteration of the nonlinear solution procedure of displacement control. Under a current value of the mixity parameter, a bilinear law is assumed, as follows:

$$\sigma = \begin{cases} k_{n0}\delta_n & \text{if} \quad \delta \leq \delta_e, \\ (1-D)\,k_{n0}\delta_n & \text{if} \quad \delta_e < \delta < \delta_f, \\ 0 & \text{if} \quad \delta \geq \delta_f, \end{cases} \tag{24}$$

$$\tau = \begin{cases} k_{t0}\delta_t & \text{if} \quad \delta \leq \delta_e, \\ (1-D)\,k_{t0}\delta_t & \text{if} \quad \delta_e < \delta < \delta_f, \\ 0 & \text{if} \quad \delta \geq \delta_f, \end{cases} \tag{25}$$

in which the damage variable D, which is a function of the mixing parameter β, is defined as follows:

$$D = D(\beta) = \frac{\delta_f\left(\delta - \delta_e\right)}{\delta\left(\delta_f - \delta_e\right)}, \tag{26}$$

where δ_e and δ_f denote, respectively, the equivalent relative displacements of the interface at the beginning of damage and complete failure. For computing δ_e and δ_f, the interaction energy criteria for both damage initiation and complete failure in mixed mode are given by:

$$\begin{cases} \left(\mathcal{G}^I/\mathcal{G}_e^I\right)^n + \left(\mathcal{G}^{II}/\mathcal{G}_e^{II}\right)^n = 1, \\ \left(\mathcal{G}^I/\mathcal{G}_c^I\right)^n + \left(\mathcal{G}^{II}/\mathcal{G}_c^{II}\right)^n = 1, \end{cases} \tag{27}$$

where $n = 1$ is assumed and $\mathcal{G}^I$, $\mathcal{G}^{II}$ are the ERR in mode I and mode II, respectively. The critical ERR in mode I and mode II are denoted by $\mathcal{G}_c^I$ and $\mathcal{G}_c^{II}$, while $\mathcal{G}_e^I$ and $\mathcal{G}_e^{II}$ are the elastic strain energies in mode I and mode II stored at the start of damage. Following [45], the projections on the pure modes of the mixed mode evolution law under the current local mixity β are assumed to be bilinear (see Fig. 8). Thus, δ_e and δ_f results:

$$\begin{cases} \delta_e = \delta_{t_e}\delta_{n_e}\sqrt{1+\beta^2}\left[\dfrac{1}{\left(\delta_{t_e}\right)^{2n} + \left(\beta\delta_{n_e}\right)^{2n}}\right]^{\frac{1}{2n}}, \\ \delta_f = \delta_{t_f}\delta_{n_f}\sqrt{1+\beta^2}\left[\dfrac{\sqrt{\left(\delta_{t_e}\right)^{2n} + \left(\beta\delta_{n_e}\right)^{2n}}}{\left(\delta_{t_e}\delta_{t_f}\right)^{n} + \left(\beta^2\delta_{n_e}\delta_{n_f}\right)^{n}}\right]^{\frac{1}{n}}, \end{cases} \tag{28}$$

where δ_{n_e} and δ_{n_f} denote the equivalent relative displacements of the interface at the beginning of the damage and complete failure in pure mode I, while δ_{t_e} and δ_{t_f} denote the equivalent relative displacements of the interface at the start of the damage and complete failure in pure mode II. The pure mode bilinear traction-separation laws are also illustrated in Fig. 8. Notice from the figure that:

$$\begin{cases} \delta_{n_e} = \sigma_{nc}/k_{n0}, & \delta_{n_f} = 2\mathcal{G}_c^I/\sigma_{nc}, \\ \delta_{t_e} = \tau_{tc}/k_{t0}, & \delta_{t_f} = 2\mathcal{G}_c^{II}/\tau_{tc}. \end{cases} \tag{29}$$

Identifying the interface parameters k_{n0}, k_{t0}, σ_{nc}, τ_{tc}, $\mathcal{G}_c^I$ and $\mathcal{G}_c^{II}$ is not a simple task, requiring experimental analysis [19,35]. Birro et al. (2020) [35] investigated the application of the CC as a method to identify these properties. First, the authors obtained the initial stiffness k_{n0} and k_{t0} of the weak interfaces assuming no-mode differentiation ($k_{n0} = k_{t0}$). Then, they used the failure initiation area S_c and the critical displacement U_c experimentally obtained in the 3PBTs to determine both the critical energy release rate $\mathcal{G}_c$ and the critical strength of the interface σ_c. Assuming the no-mode differentiation condition, Eq. (29) is simplified by $\delta_e = \delta_{n_e} = \delta_{t_e}$ and $\delta_f = \delta_{n_f} = \delta_{t_f}$, as well as $\sigma_{nc} = \tau_{tc}$ and $\mathcal{G}_c^I = \mathcal{G}_c^{II} = \mathcal{G}_c$.

According to Martin et al. (2016) [15], the practical application of TSM requires a mesh that is sufficiently fine to accurately resolve the cohesive length. They suggest the following condition for the length of the mesh L_{mesh}:

$$\frac{6}{\pi}\frac{L_{\text{mesh}}}{h_s} < \frac{L_c}{h_s} < \frac{1}{20}\frac{E_a}{\sigma_c}. \tag{30}$$

Here, E_a represents the Young modulus of the adhesive and L_c represents the length of the fracture process zone, which is defined according

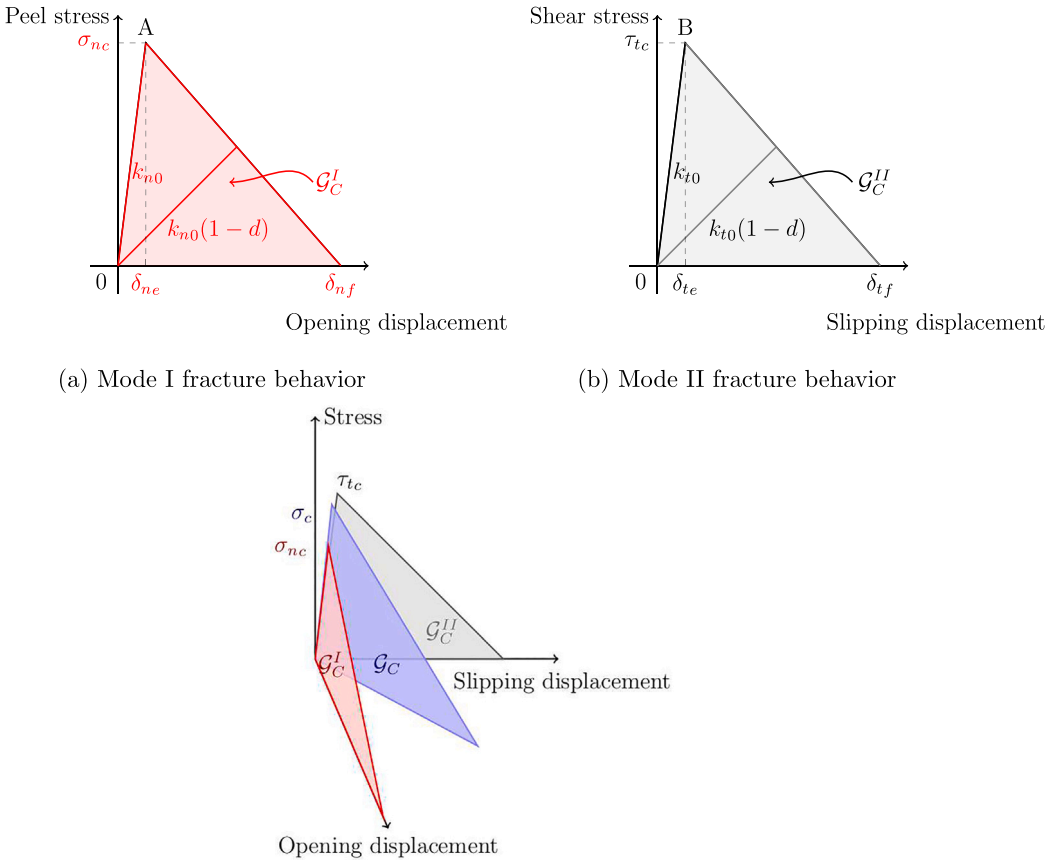

(a) Mode I fracture behavior

(b) Mode II fracture behavior

(c) Mixed-mode fracture envelope

Fig. 8. Traction-separation laws: (a) in pure mode I, (b) in pure mode II, (c) under mixed-mode.

to the mechanical properties of the interface as follows:

$$L_c = \frac{E_a \mathcal{G}_c}{\sigma_c^2}. \tag{31}$$

5. Boundary element models

This section presents a short overview of the boundary element formulation used in this work. The weak interface modeling strategy and the progressive damage formulation derive from [27]. However, in the present work, the single domain dual BEM [46] is replaced by the well-known multizone formulation [47] to account for the different materials in the substrate-adhesive systems. In addition, the Park–Paulino–Roesler traction-separation relationship is replaced by the progressive traction-separation law described in Section 4.4.

5.1. Governing boundary integral equations

The linearized governing equations of an elastic solid can be represented in terms of the displacement BIE [48]. Assuming nil body forces, the displacement BIE is written for a boundary source point $\mathbf{x}'$ as follows:

$$\mathbf{c}\left(\mathbf{x}'\right)\mathbf{u}\left(\mathbf{x}'\right) + C\int_\Gamma \mathbf{t}^*\left(\mathbf{x}',\mathbf{x}\right)\mathbf{u}(\mathbf{x})\mathrm{d}\Gamma = \int_\Gamma \mathbf{u}^*\left(\mathbf{x}',\mathbf{x}\right)\mathbf{t}(\mathbf{x})\mathrm{d}\Gamma, \tag{32}$$

where $\mathbf{x}'$ and $\mathbf{x}$ are the source and field points, $\mathbf{u}(\mathbf{x}')$ indicates the displacement at the source point, $\mathbf{u}(\mathbf{x}) = u_i\mathbf{e_i}$ and $\mathbf{t}(\mathbf{x}) = t_i\mathbf{e_i}$ represent the displacement and traction boundary fields, and $\mathbf{u}^*(\mathbf{x}',\mathbf{x}) = u_{ij}(\mathbf{x}',\mathbf{x})\mathbf{e_i}\otimes\mathbf{e_j}$ and $\mathbf{t}^*(\mathbf{x}',\mathbf{x}) = t_{ij}(\mathbf{x}',\mathbf{x})\mathbf{e_i}\otimes\mathbf{e_j}$ are the Kelvin fundamental solutions for displacements and tractions. The *Cauchy* principal value integral is indicated by $C\int$ and $\mathbf{c}(\mathbf{x}')\mathbf{u}(\mathbf{x}')$ is the free term arising from the singular integral.

5.2. Weak interfaces: stress and displacement discontinuity vectors

For convenience and without loss of generality, the weak interface stress vector $\vec{t}$ can be related to the vector of displacement discontinuities $\vec{\delta}$ by:

$$\vec{t} = \mathbf{k}\vec{\delta} \tag{33}$$

where

$$\mathbf{k} = \begin{bmatrix} k_{n0} & \\ & k_{t0} \end{bmatrix} \tag{34}$$

stands for the local initial stiffness matrix of the weak interface. Let

$$\mathbf{R} = \begin{bmatrix} \vec{e}_n & \vec{e}_t \end{bmatrix} \tag{35}$$

be the orthogonal transformation that relates the local system nt of the interface to the global analysis system xy. Thus,

$$\vec{\delta}_c = \mathbf{R}\vec{\delta} \quad \text{and} \quad \vec{t}_c = \mathbf{R}\vec{t} \tag{36}$$

are the vector of displacement discontinuities and the stress vector of the weak interface expressed in the global system, respectively. Since $\mathbf{R}$ is orthogonal,

$$\vec{t}_c = \mathbf{k}_c\vec{\delta}_c\,, \qquad \mathbf{k}_c = \mathbf{R}\mathbf{k}\mathbf{R}^T, \tag{37}$$

where $\mathbf{k}_c$ is the global stiffness matrix.

5.3. Boundary discretization and weak interface modeling

The discretization of the boundaries and interfaces into boundary elements with linear approximations for the displacement and traction

fields, and the imposition by collocation of Eq. (32) allows to obtain a linear system of equations given by:

$$\mathbf{HU} = \mathbf{GT}. \tag{38}$$

The dense square matrices $\mathbf{H}$ and $\mathbf{G}$ arise from the integration of the kernels, whereas the column matrices $\mathbf{U}$ and $\mathbf{T}$ collect, respectively, the coefficients $\mathbf{u}^e_\alpha$ and $\mathbf{t}^e_\alpha$ from the displacement and traction approximations $\mathbf{u}^e = N^e_\alpha \mathbf{u}^e_\alpha$ and $\mathbf{t}^e = N^e_\alpha \mathbf{t}^e_\alpha$ over the boundary elements e. Singular integrals are regularized herein by the subtraction singularity technique [48]. Discontinuous boundary elements are adopted in regions of geometric or traction discontinuities. Regarding the position of the elements on the boundary and interfaces: $\Gamma^e \in \Gamma_u$, $\Gamma^e \in \Gamma_t$, $\Gamma^e \in \Gamma_{c+}$ and $\Gamma^e \in \Gamma_{c-}$, in which Γ_u, Γ_t, Γ_{c+} and Γ_{c-} represent Dirichlet boundary, Neumann boundary and sides + and − of the interface, Eq. (38) can be split as:

$$\begin{bmatrix}\mathbf{H}_u & \mathbf{H}_t & \mathbf{H}_{c+} & \mathbf{H}_{c-}\end{bmatrix}\begin{Bmatrix}\lambda\overline{\mathbf{U}}\\ \mathbf{U}_t\\ \mathbf{U}_{c+}\\ \mathbf{U}_{c-}\end{Bmatrix} = \begin{bmatrix}\mathbf{G}_u & \mathbf{G}_t & \mathbf{G}_{c+} & \mathbf{G}_{c-}\end{bmatrix}\begin{Bmatrix}\mathbf{T}_u\\ \lambda\overline{\mathbf{T}}\\ \mathbf{T}_{c+}\\ \mathbf{T}_{c-}\end{Bmatrix} \tag{39}$$

where $\overline{\mathbf{U}}$ and $\overline{\mathbf{T}}$ are prescribed displacement and traction patterns and λ is a load factor.

Defining the global displacement discontinuity $\Delta_c = \mathbf{U}_{c+} - \mathbf{U}_{c-}$, imposing the balance of interface tractions $\mathbf{T}_{c+} + \mathbf{T}_{c-} = \mathbf{0}$, and imposing the weak interface model $\mathbf{T}_{c+} = \mathbf{K}_c \Delta_c$, in which

$$\mathbf{K}_c = \begin{bmatrix}\mathbf{k}_c^1 & & \\ & \ddots & \\ & & \mathbf{k}_c^{N_c}\end{bmatrix} \tag{40}$$

is the assembled cohesive stiffness matrix and $\mathbf{k}_c^i$ $(i = 1, \ldots, N_c)$ are the global initial stiffness matrices for the nodes i at the interface, it is possible to obtain the final system of equations of the weak interface problem:

$$\mathbf{AX} = \lambda\overline{\mathbf{B}}, \tag{41}$$

where the square matrix $\mathbf{A}$ and the column matrices $\overline{\mathbf{B}}$ and $\mathbf{X}$ are:

$$\mathbf{A} = \begin{bmatrix}\mathbf{H}_t & -\mathbf{G}_u & \left(\mathbf{H}_{c+} + \mathbf{H}_{c-}\right) & \left[\mathbf{H}_{c+} + \left(\mathbf{G}_{c-} - \mathbf{G}_{c+}\right)\mathbf{K}_c\right]\end{bmatrix}, \tag{42}$$

and

$$\overline{\mathbf{B}} = \begin{bmatrix}\mathbf{G}_t & -\mathbf{H}_u\end{bmatrix}\begin{Bmatrix}\overline{\mathbf{T}}\\ \overline{\mathbf{U}}\end{Bmatrix}, \qquad \mathbf{X} = \begin{Bmatrix}\mathbf{U}_t\\ \mathbf{T}_u\\ \mathbf{U}_{c-}\\ \Delta_c\end{Bmatrix}. \tag{43}$$

5.4. Undertaken approach for linear elastic propagation

Once the fracture properties $\mathcal{G}_c$ and σ_c are determined by the CC (see Remark 1), the incremental propagation of the crack based on LEFM can be analyzed using Griffith theory, as described in Section 4.3. The structural load–displacement response of the 3PBT can be easily obtained from incremental linear elastic crack propagation according to Eq. (21). Fig. 9 illustrates a cracked weak interface for an intermediary step of propagation of symmetric (a) and asymmetric (b) cracking.

The modeling of a weakly cracked interface does not change the final system in Eq. (41). The only change required is based on the evaluation of the local stiffness matrix of the nodes i lying on the traction-free crack

$$\mathbf{k}_c^i = \mathbf{R}^i \mathbf{k}^i \mathbf{R}^{iT}, \tag{44}$$

which are now computed from the degraded stiffness matrix $\mathbf{k}^i$ given by:

$$\mathbf{k}^i = \begin{bmatrix}(1-D)\,k_{n0} & \\ & (1-D)\,k_{t0}\end{bmatrix} = \begin{bmatrix}10^{-6}k_{n0} & \\ & 10^{-6}k_{t0}\end{bmatrix}, \tag{45}$$

in which $(1 - D) = 10^{-6}$ is set as a constant to characterize complete interface failure (traction-free cracks) and avoid numerical instabilities.

5.5. Undertaken approach for progressive damage modeling

The bilinear traction-separation law adopted for the progressive damage analysis can be written as:

$$\sigma = k_n(\delta)\,\delta_n = \begin{cases} k_{n0}\delta_n, & \text{if} \quad \delta \le \delta_e, \\ (1-D)\,k_{n0}\delta_n, & \text{if} \quad \delta_e < \delta < \delta_f, \\ 10^{-6}k_{n0}\delta_n, & \text{if} \quad \delta \ge \delta_f, \end{cases} \tag{46}$$

$$\tau = k_t(\delta)\,\delta_t = \begin{cases} k_{t0}\delta_t, & \text{if} \quad \delta \le \delta_e, \\ (1-D)\,k_{t0}\delta_t, & \text{if} \quad \delta_e < \delta < \delta_f, \\ 10^{-6}k_{t0}\delta_t, & \text{if} \quad \delta \ge \delta_f, \end{cases} \tag{47}$$

in which

$$D = D(\delta) = \frac{\delta_f\left(\delta - \delta_e\right)}{\delta\left(\delta_f - \delta_e\right)}, \quad \text{and} \quad \delta = \sqrt{\delta_n^2 + \delta_t^2}. \tag{48}$$

It should be noted that activation of the damage variable D (for $\delta > \delta_e$) in a single interface node i is sufficient to cause the dependency $\mathbf{k}_c^i = \mathbf{k}_c^i(\delta^i)$. Therefore, the dependency $\mathbf{K_c} = \mathbf{K_c}(\Delta_c)$ introduces nonlinearity to the system in Eq. (41). For a non-equilibrated state of unknowns $(\mathbf{X}, \lambda)$, the residue vector $(\boldsymbol{\mathcal{R}})$ can be defined as:

$$\boldsymbol{\mathcal{R}}(\mathbf{X}, \lambda) = \mathbf{AX} - \lambda\overline{\mathbf{B}}. \tag{49}$$

In what follows, the adopted solution procedure is briefly described, selecting the j−th component of $\mathbf{X}$ to control the continuation of the solution. Let

$$\boldsymbol{\mathcal{R}}_i = \mathbf{AX}_i - \lambda_i\overline{\mathbf{B}} \neq \mathbf{0} \tag{50}$$

be the residue for the current solution guess $(\mathbf{X}_i, \lambda_i)$. An improved solution is achieved by the update

$$\mathbf{X}_{i+1} = \mathbf{X}_i + \Delta\mathbf{X}_i \quad \text{and} \quad \lambda_{i+1} = \lambda_i + \Delta\lambda_i, \tag{51}$$

until the norm of the residue becomes small enough. The increments $\Delta\mathbf{X}_i$ and $\Delta\lambda_i$ are obtained by setting

$$\Delta\mathbf{X}_i = \Delta\mathbf{X}_i^c - \Delta\lambda_i\Delta\mathbf{X}_i^p \tag{52}$$

and

$$\left[\boldsymbol{\mathcal{R}}_i + \left.\frac{\partial\boldsymbol{\mathcal{R}}}{\partial\mathbf{X}}\right|_i \Delta\mathbf{X}_i^c\right] - \left[\left.\frac{\partial\boldsymbol{\mathcal{R}}}{\partial\mathbf{X}}\right|_i \Delta\mathbf{X}_i^p + \overline{\mathbf{B}}\right]\Delta\lambda_i = \mathbf{0}. \tag{53}$$

The previous relation is satisfied if the bracketed terms are null, then

$$\left.\frac{\partial\boldsymbol{\mathcal{R}}}{\partial\mathbf{X}}\right|_i \Delta\mathbf{X}_i^c = -\boldsymbol{\mathcal{R}}_i \quad \text{and} \quad \left.\frac{\partial\boldsymbol{\mathcal{R}}}{\partial\mathbf{X}}\right|_i \Delta\mathbf{X}_i^p = -\overline{\mathbf{B}}, \tag{54}$$

which enable determining the terms $\Delta\mathbf{X}_i^c$, $\Delta\mathbf{X}_i^p$ after solving the above linear systems. Since the j−th component of $\mathbf{X}$ is controlled, $\mathbf{e}_j^T\Delta\mathbf{X}_i = 0$, and thus $\mathbf{e}_j^{\mathrm{T}}\Delta\mathbf{X}_i = 0$, which gives

$$\Delta\lambda_i = -\frac{\mathbf{e}_j^{\mathrm{T}}\Delta\mathbf{X}_i^c}{\mathbf{e}_j^{\mathrm{T}}\Delta\mathbf{X}_i^p}. \tag{55}$$

This accomplishes the iterative update of the solution. The derivation of the tangent matrix $\partial\boldsymbol{\mathcal{R}}/\partial\mathbf{X}$ and more details on how to account for all possible interface surface conditions: (i) contact, (ii) softening, (iii) unloading/reloading and (iv) complete failure, can be found in [27].

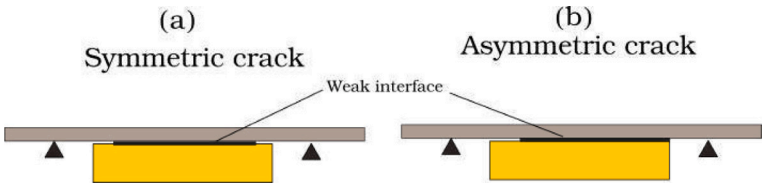

Fig. 9. Cracked weak interface: (a) symmetric and (b) asymmetric propagation.

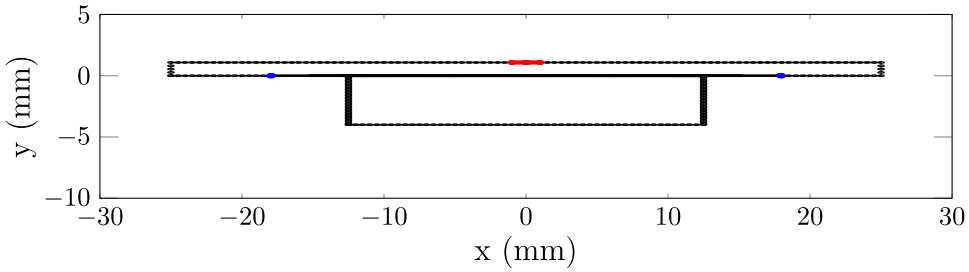

Fig. 10. Boundary element mesh adopted for the substrate-adhesive system $h_s = 1.08$ mm.

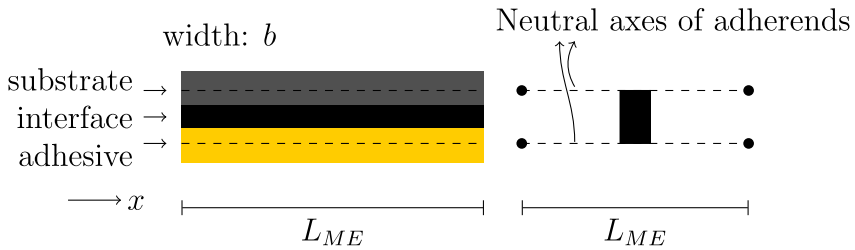

Fig. 11. Representation of a ME: substrate, interface, and adhesive.

6. Results

In this section, the quantitative methodology proposed herein to access the critical stress and the fracture toughness of adhesive interfaces using BEM models and the CC is validated. The methodology is validated with the experimental results from the two substrate-adhesive systems described in Section 3 and with a subsequent progressive damage analysis based on the traction-separation law described in Section 4.4. The undertaken analyses considered four different situations: (i) propagation of two symmetric cracks at the substrate-adhesive interface with substrate thickness $h_s = 1.08$ mm; (ii) propagation of two symmetric cracks at the substrate-adhesive interface with substrate thickness $h_s = 1.62$ mm; (iii) asymmetric propagation of a single crack at the substrate-adhesive interface with substrate thickness $h_s = 1.08$ mm; and (iv) asymmetric propagation of a single crack at the substrate-adhesive interface with substrate thickness $h_s = 1.62$ mm. More or less severe snap-back instabilities may occur in the force–displacement response of the problem depending on the situation considered. The cohesive surface conditions discussed in [27]: (i) contact, (ii) softening, (iii) unloading/reloading, and (iv) complete failure, are indispensable to solve the problems, especially in the case of asymmetric crack propagation.

6.1. Validation of BEM models with other solutions

The boundary element mesh adopted for the plane stress BEM models was defined based on a convergence study presented in Appendix. The mesh is composed of 1486 elements of linear approximation, which include 1152 weak interface elements, 576 on each side. The initial 0.125 mm on both left and right sides of the adhesive-substrate interface are discretized using a very fine mesh of 180 elements (720 elements/mm) to accurately capture the crack initiation according to the CC. The remaining 24.75 mm are discretized with 396 elements (16 elements/mm). Gradual refinement is also adopted in regions near the corner at the beginning of the adhesive-substrate interface. The boundary element mesh adopted for the substrate-adhesive system with substrate thickness $h_s = 1.08$ mm is illustrated in Fig. 10. A similar mesh, with the same number of elements, is adopted for the substrate-adhesive system with substrate thickness $h_s = 1.62$ mm.

The boundary conditions are the following: (i) right fixed and left rolling supports, which are modeled by fixing the displacements of the boundary elements in blue in Fig. 10 (u_x and u_y for the fixed support and u_y for the rolling support); (ii) applied vertical load, which is modeled by controled displacements $\lambda\bar{u}_y$ for the boundary elements in red in Fig. 10. The size of the applied load region is 2.0 mm, the size of the supports is 0.12 mm, and the length between the centers of the supports is 35.90 mm.

Notice that even though a very fine mesh is required at the interface to capture with precision the initial crack according to the CC, the mesh reduction property of the BEM avoids the spread of such a level of refinement throughout the domain.

To validate the BEM models, the peel and shear stresses along the undamaged interface for both substrate-adhesive systems are compared with existing solutions from the literature. First, the semi-analytical method known as the macro-element (ME) approach is used as a first reference [35]. This method employs a four-node element of length L_{ME} to represent the substrate, adhesive, and interface, as illustrated in Fig. 11.

The width of the ME, denoted as b in Fig. 11, is set to b_2, which corresponds to the width of the adhesive. To ensure equivalency, Birro et al. (2020) [35] adjusted Young's modulus of the plate by the ratio b_2/b_1. In this model, adhesives and substrates are represented as Timoshenko beams, and their kinematics are coupled by an infinite number of springs subjected to shear and peel modes, calculated on the basis

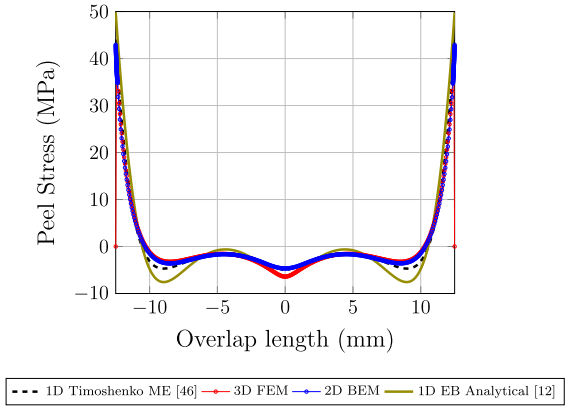

Fig. 12. Peel stress over the undamaged interface: $h_s = 1.08$ mm.

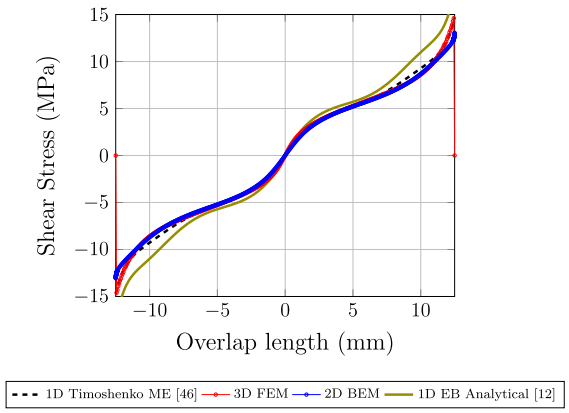

Fig. 13. Shear stress over the undamaged interface: $h_s = 1.08$ mm.

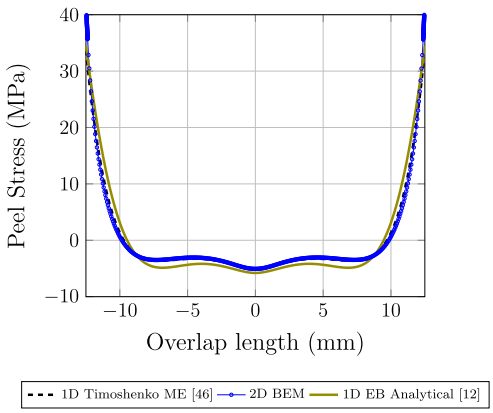

Fig. 14. Comparison of peel Stress over the undamaged interface: $h_s = 1.62$ mm.

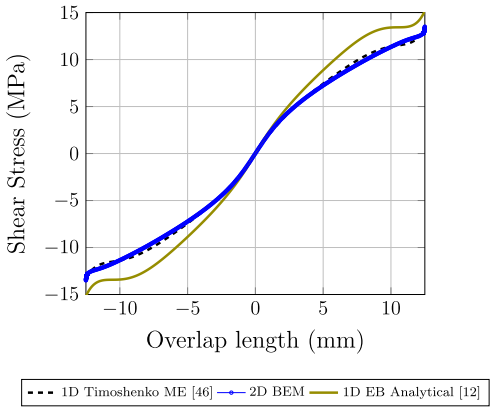

Fig. 15. Comparison of shear stress over the undamaged interface: $h_s = 1.62$ mm.

of the Goland and Reissner hypothesis. Although the ME approach was inspired by the FEM, it does not assume any interpolation functions. Instead, these functions are derived as solutions to the governing differential equations. After computing the stiffness matrix for each ME, the total stiffness matrix of the structure is assembled, and the solution is obtained by minimizing the potential energy. More recently, Birro et al. (2024) [12] introduced an analytical solution to determine the peel and shear stress distributions using a weak interface formulation and a 1D Euler–Bernoulli (EB) approach. Specifically, a unique numerical method is employed to compute the integration constants of these equations.

Figs. 12 and 13 present, respectively, the peel and shear stresses along the undamaged interface for the substrate-adhesive system with $h_s = 1.08$ mm. On the other hand, Figs. 14 and 15 present, respectively, the peel and shear stresses along the undamaged interface for the substrate adhesive system with $h_s = 1.62$ mm.

Notice that the BEM solution agrees well with the 1D Timoshenko ME solution for both substrate thicknesses.

6.2. Fracture parameters assessment by the CC

In order to employ the CC, defined in Eqs. (11), to assess the fracture parameters, it is necessary to calculate the functions $K(S)$ and $\bar{A}(S)$, which depend on the size S of the crack. Notice that, since the width of the substrate-adhesive interface is constant, $b = 5$ mm, and the 2D crack propagation analysis is adopted, the cracked size is equal to $S = ab$ for asymmetrical propagation cases and $S = 2ab$ for symmetrical propagation cases. In both cases, S is linearly dependent on the length of the crack a.

The function $K(S)$ is defined from Eq. (11) as $K(S) = \sigma_{\text{eq}}(S)/U$, in which U is the prescribed displacement and $\sigma_{\text{eq}}(S) = \sqrt{\sigma^2 + \tau^2}$ is the equivalent stress calculated from the peel σ and shear τ stresses presented in the previous subsection. The equivalent stiffness functions $K(S)$ for both substrate-adhesive systems $h_s = 1.08$ mm and $h_s = 1.62$ mm are illustrated in Fig. 16.

The function $\bar{A}(S)$ on the other hand is defined as $\bar{A}(S) = \mathcal{G}_{inc}(S)/U^2$, in which $\mathcal{G}_{inc}(S)$ is the IERR defined in Eq. (9). From linear analysis with $S = 0$ and with $S > 0$ it is possible to compute discrete values for the function $\mathcal{G}_{inc}(S)$, where the energy variation ΔW is represented by the red area shown in Fig. 17.

Through the incremental linear elastic crack propagation analysis described in Section 5.4 it is possible to obtain the function $\mathcal{G}_{inc}(S)$ in a discrete form, which subsequently allows the determination of $\bar{A}(S)$. Fig. 18 presents the results $\bar{A}(S)$ for the substrate-adhesive system $h_s = 1.08$ mm with respect to both the symmetric and the asymmetric crack propagation conditions. On the other hand, Fig. 19 presents the $\bar{A}(S)$ results for the substrate-adhesive system $h_s = 1.62$ mm also with respect to both propagation conditions.

Based on the previously defined discrete functions $K(S)$ and $\bar{A}(S)$ and knowing from Table 1 the critical crack sizes, $S_c = 0.102$ mm^2 for $h_s = 1.08$ mm and $S_c = 0.07$ mm^2 for $h_s = 1.62$ mm, it is possible to

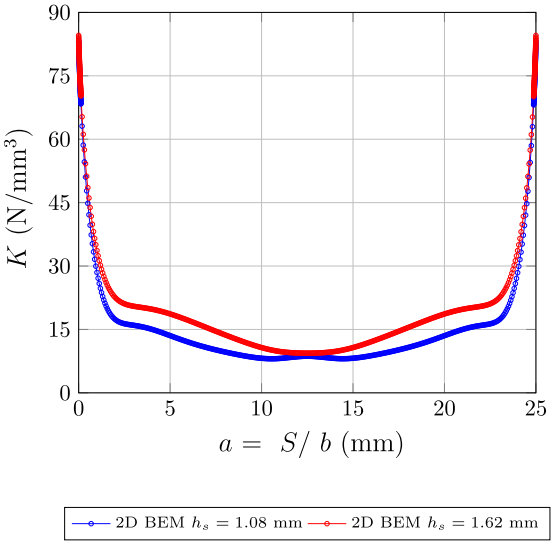

Fig. 16. Equivalent stiffness over the undamaged interface for h_s = 1.08 mm (blue) and h_s = 1.62 mm (red).

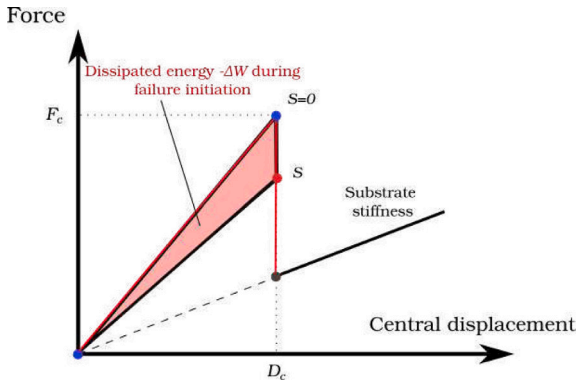

Fig. 17. Incremental energy release rate computation.

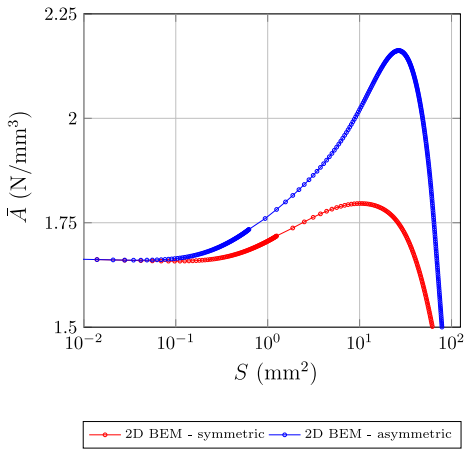

Fig. 18. Function $\bar{A}(S)$ for both symmetric and asymmetric cracks: h_s = 1.08 mm.

assess the critical stress σ_c and the fracture toughness $\mathcal{G}_c$ of the interface for both substrate-adhesive systems using the CC equations. Table 4 presents the fracture parameters for the substrate-adhesive system with h_s = 1.08 mm.

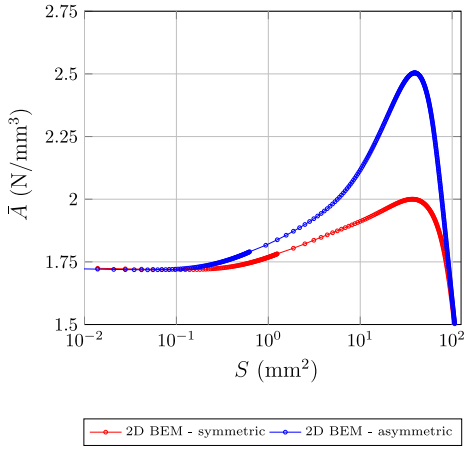

Fig. 19. Function $\bar{A}(S)$ for both symmetric and asymmetric cracks: h_s = 1.62 mm.

Table 4
Fracture parameters assessment: h_s = 1.08 mm.

Crack	$K(S_c)$	$\bar{A}(S_c)$	σ_c	$\mathcal{G}_c$
Symmetric	79.882 N/mm^3	1.658 N/mm^3	44.654 MPa	0.518 N/mm
Asymmetric	79.882 N/mm^3	1.664 N/mm^3	44.654 MPa	0.520 N/mm

Table 5
Fracture parameters assessment: h_s = 1.62 mm.

Crack	$K(S_c)$	$\bar{A}(S_c)$	σ_c	$\mathcal{G}_c$
Symmetric	82.121 N/mm^3	1.719 N/mm^3	45.906 MPa	0.5371 N/mm
Asymmetric	82.121 N/mm^3	1.719 N/mm^3	45.906 MPa	0.5371 N/mm

Notice that almost the same values of σ_c and $\mathcal{G}_c$ were obtained, regardless of the propagation condition of the crack. Similarly, Table 5 presents the fracture parameters for the substrate-adhesive system with h_s = 1.62 mm. Again, almost the same values of σ_c and $\mathcal{G}_c$ were obtained, regardless of the propagation condition of the crack.

Although all configurations analyzed in this work share the same substrate/adhesive system, slight variations in the obtained fracture parameters ($\mathcal{G}_c$ and σ_c) are expected and justified by the methodology employed. The fracture properties were extracted through an inverse analysis using the CC, which is sensitive to experimental input such as maximum force, stiffness, and contact area - each subject to inherent variability. Consequently, the reported fracture parameters naturally reflect the propagation of experimental uncertainty. The relative variation observed between configurations (approximately 3.6% for $\mathcal{G}_c$ and 2.8% for σ_c) remains within acceptable engineering limits. This behavior is consistent with findings in the literature, where minor differences were also observed between configurations with the same material system due to factors such as geometric configuration, local stress distribution, or measurement uncertainty [49,50]. Furthermore, according to Muñoz-Reja et al. (2017) [51], even when using the same material system, slight differences in energy release rates and remote stresses can occur between symmetric and asymmetric configurations. However, it is important to note that the stress criterion in the CC is evaluated based on the non-cracked configuration and thus remains unaffected by the symmetry of the debonding. This highlights that while geometric configuration may slightly influence the energetic response, the fundamental stress-based criterion is essentially the same between symmetrical and asymmetrical configurations and thus configuration independent.

To better understand the structural behavior during the onset of the failure, the normalized functions f_σ and $f_\mathcal{G}$ of the CC are plotted in Fig. 20 for the thickness of the substrate h_s = 1.08 mm for both symmetric

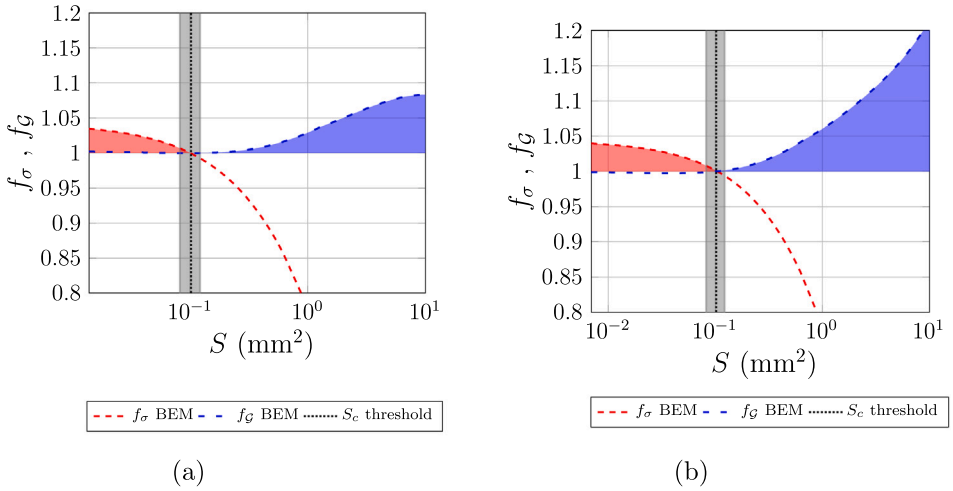

Fig. 20. Comparison of normalized functions f_σ and $f_\mathcal{G}$ with respect to crack area S for (a) symmetrical and (b) asymmetrical configurations for $h_s = 1.08$ mm.

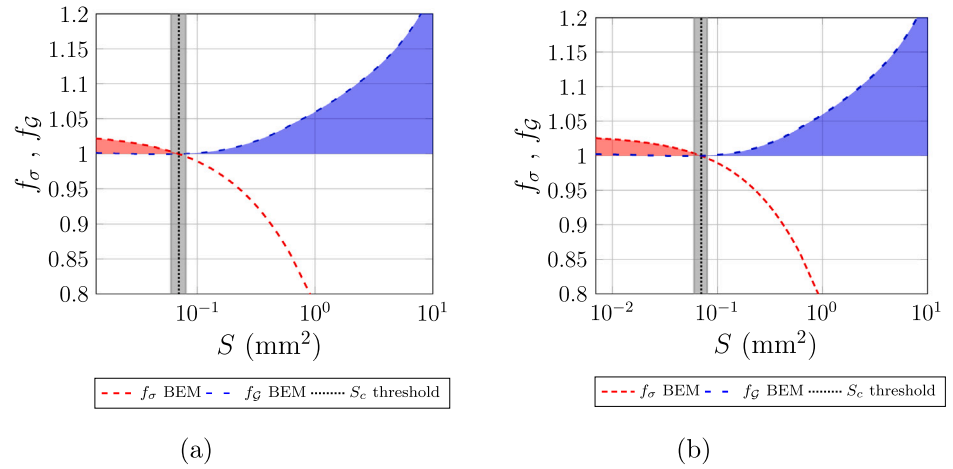

Fig. 21. Comparison of normalized functions f_σ and $f_\mathcal{G}$ with respect to crack area S for (a) symmetrical and (b) asymmetrical configurations for $h_s = 1.62$ mm.

and asymmetric configurations. The vertical gray widthband denotes the value of S_c with the standard deviation found by [35]. As can be seen, a small variation provoked by the uncertainty of the measurement has a minor effect on the ERR, which has also been observed using ME and confirmed now using the BEM formulation. The red and blue areas denote the zones where the stress and energy criteria are respected.

In the same way, the curves f_σ and $f_\mathcal{G}$ are plotted for $h_s = 1.62$ mm for symmetric and asymmetric configurations (see Fig. 21), and a similar behavior is retrieved.

It is important to note that both the 1D Timoshenko ME and the 3D FE results presented in Section 6.1 are derived from mesh convergence studies, which are fully detailed in [35,52], respectively. The good agreement between the BEM results and the 1D-ME/3D FEM results (see Figs. 12, 13, 14, 15) in selected cases supports the robustness of the BEM implementation and further corroborates the accuracy of the BEM results reported in Section 6.2.

6.3. Progressive damage analysis

In the following, the interface fracture properties assessed in Section 6.2 are employed to evaluate the structural response of 3PBT performed on substrate-adhesive systems. The load–displacement responses are obtained by using the Algorithm 2 presented in [50], which uses the linear elastic crack propagation BEM results, and by using the progressive damage BEM model described in Section 5.5. The

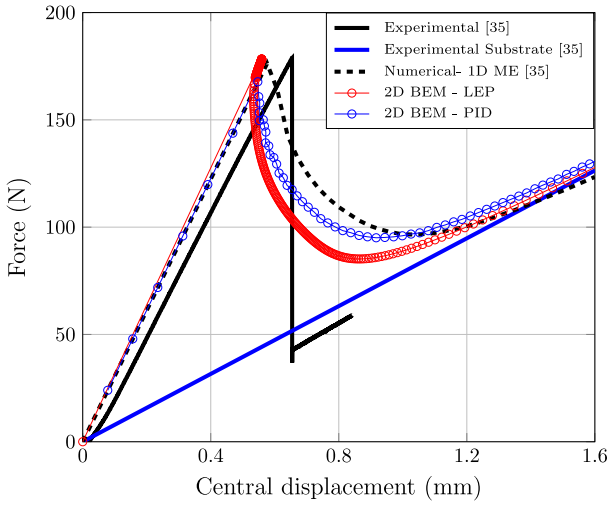

Fig. 22. Force–displacement results for symmetric debonding: $h_s = 1.08$ mm.

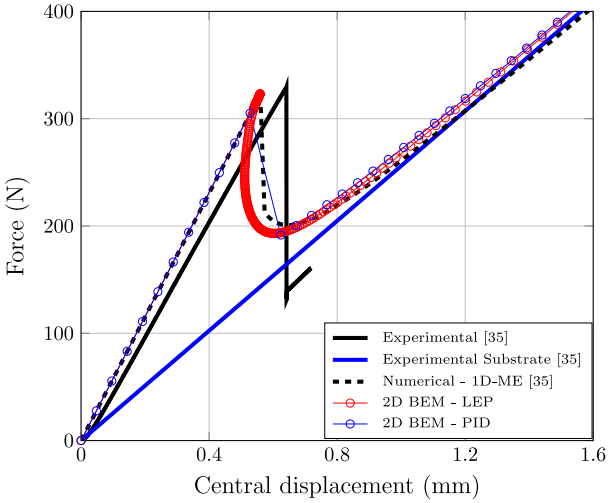

Fig. 23. Force–displacement results for symmetric debonding: $h_s = 1.62$ mm.

validation of the interface fracture properties is achieved by comparing obtained the load–displacement responses with the experimental and numerical responses reported in [50].

Regarding the mesh condition presented in Eq. (30) and based on Tables 4 and 5, the minimal mesh length required is $L_{mesh} \leq 0.4$ mm. The mesh shown in Fig. 10 and used for the CC analysis respects this criterion, since the mesh density is 1/16 for the coarser region.

6.3.1. Case 1: symmetric debonding

The load–displacement responses of the substrate-adhesive systems $h_s = 1.08$ mm and $h_s = 1.62$ mm are presented herein regarding the symmetric debonding of the adhesive. The fracture parameters adopted were those presented in Tables 4 and 5. Figs. 22 and 23 present, respectively, the load–displacement responses of the substrate-adhesive systems $h_s = 1.08$ mm and $h_s = 1.62$ mm, obtained with the linear elastic propagation (LEP) analysis and with the progressive interface damage (PID) analysis. The experimental and numerical results, using the 1D ME - Timoshenko, from [50] are also illustrated.

The nonlinear progressive damage analysis was performed by prescribing in 50 load steps the vertical displacement $u_y = -2.4$ mm at the middle nodes of the upper surface of the 3PBTs. The tolerance for convergence was established as 10^{-3} and an energy-based convergence criterion was used [27]. Notice from Figs. 22 and 23 that the responses obtained in the present work are very close to the numerical response provided by [50]. The numerical critical loads are similar to the experimental ones. However, the post-peak experimental results deviate from the numerical counterparts.

Figs. 24 and 25 illustrate, respectively, the deformed configuration of the substrate-adhesive systems $h_s = 1.08$ mm and $h_s = 1.62$ mm for an intermediary step on a scale 1:1. Notice that the deformed configuration C_n is relatively different from the unreformed one C_0, indicating that nonlinear geometric effects may affect the response and justify the differences in the numerical and experimental results.

6.3.2. Case 2: asymmetric debonding

The load–displacement responses of the substrate-adhesive systems $h_s = 1.08$ mm and $h_s = 1.62$ mm are presented herein now regarding the asymmetric adhesive debonding. The fracture parameters adopted were those presented in Tables 4 and 5. Figs. 26 and 27 present, respectively, the load–displacement responses of the substrate-adhesive systems $h_s = 1.08$ mm and $h_s = 1.62$ mm, obtained with both the LEP and the PID analysis.

To model asymmetric progressive damage debonding analysis, the critical stress of the first 128 elements on the right side of the substrate-adhesive interface was set equal to $\sigma_c = 10^{50}$ MPa to ensure that damage does not occur from this side. The nonlinear progressive damage analysis was performed by prescribing in 50 load steps the vertical displacement $u_y = -2.4$ mm at the middle nodes of the upper surface of the 3PBTs. The same convergence criterion and tolerance adopted for the symmetric debonding case were considered. Although there are no reference responses for the asymmetric debonding case, the similarity between the load–displacement responses obtained with both the LEP and the PID approaches corroborates the validity of the model.

Figs. 28 and 29 illustrate, respectively, the deformed configuration of the substrate-adhesive systems $h_s = 1.08$ mm and $h_s = 1.62$ mm for an intermediary step on a scale 1:1. Notice that once again the deformed configuration C_n is relatively different from the unreformed one C_0, which indicates that geometrically nonlinear effects may affect the response and justify the differences in the numerical and experimental results.

The analyses demonstrate that an asymmetric configuration appears to be more suitable than a symmetric one, as more unstable failure propagation is obtained, corresponding to the experimental behavior.

The observed discrepancies between experimental and numerical post-peak responses, particularly in Figs. 22 and 23, are consistent with limitations previously reported in similar modeling approaches based on traction-separation laws [15,35]. Although the model accurately predicts global quantities such as peak force and general failure trends, post-peak behavior remains more difficult to reproduce due to the complexity of the underlying failure mechanisms, including rapid crack propagation, material softening, and instability phenomena. These differences are especially noticeable in the trajectory and magnitude of post-peak softening, which are highly sensitive to local effects that are not fully resolved in the current formulation. Although the model operates within a linear kinematic framework, non-symmetric failure propagation introduces severe snap-back effects, which the LEP BEM analysis were capable of reproducing, enhancing agreement with experimental trends in Figs. 26 and 27. However, this does not fully resolve the post-peak mismatch. The PID BEM analyzes were unable to reproduce the unstable part of the force–displacement response, due to the fact that the nonlinear solver used is a displacement control Newton-based method.

Regarding PID modeling, the overall behavior of the force displacement curves seems very similar for both symmetric and asymmetric failure propagations. For a deeper analysis, the evolution of the crack length versus the prescribed displacement is shown in Figs. 30 and 31 for all the aforementioned configurations. Although the mesh quality condition is respected, precaution is necessary when comparing the PID and the CC for unstable propagation. In addition to the strength and fracture toughness required as inputs, a third parameter intervenes in the PID: the traction-opening displacement profile. Although this profile has a relatively minor impact on the force–displacement response in brittle failures (except near the maximum force associated with crack initiation), it primarily affects dynamic phenomena such as crack initiation, branching, and unstable propagation. However, similar results are obtained regardless of the traction-opening displacement profile in the case of stable rectilinear crack propagation, provided that the characteristic length is small relative to the dimensions of the sample [49,53]. The results in Figs. 30 and 31 suggests that the PID propagation of symmetric failures has a significant impact on the behavior of the crack length-displacement curve when compared to the LEP case.

The proposed BEM-CC framework offers a new and effective approach to analyze adhesive failure by combining both approaches. In addition, CC-based analysis helps determine PID input values, enabling a direct comparison between the two methods. In the context of asymmetric crack propagation, very good agreement is observed between both approaches, owing in large part to the brittle behavior

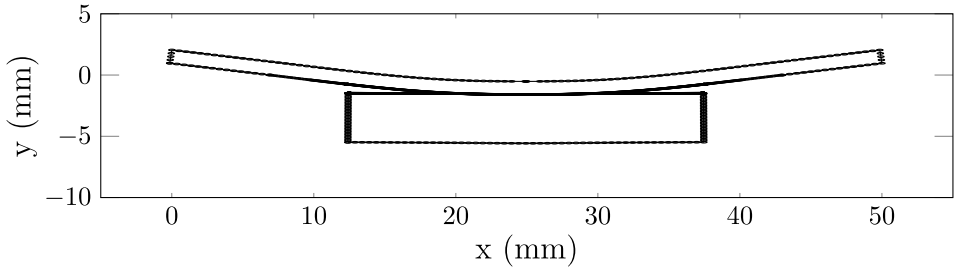

Fig. 24. C_n configuration for symmetric debonding: $h_s = 1.08$ mm for an intermediary step.

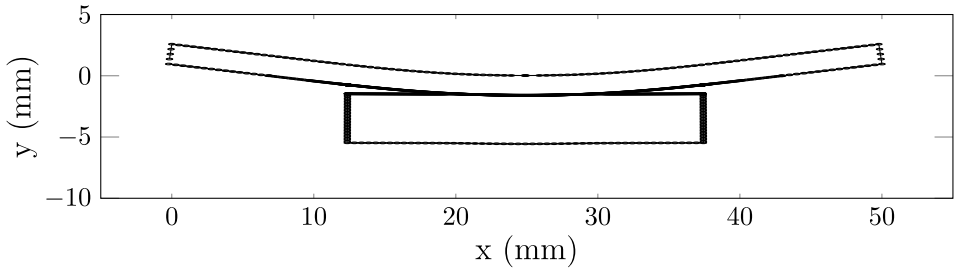

Fig. 25. C_n configuration for symmetric debonding: $h_s = 1.62$ mm for an intermediary step.

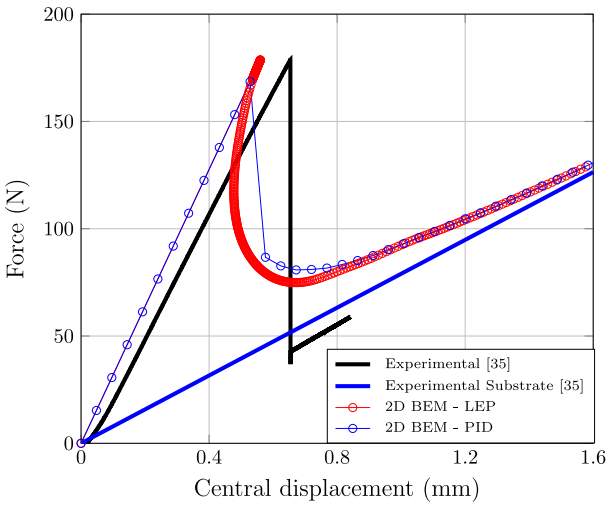

Fig. 26. Force–displacement results for asymmetric debonding: $h_s = 1.08$ mm.

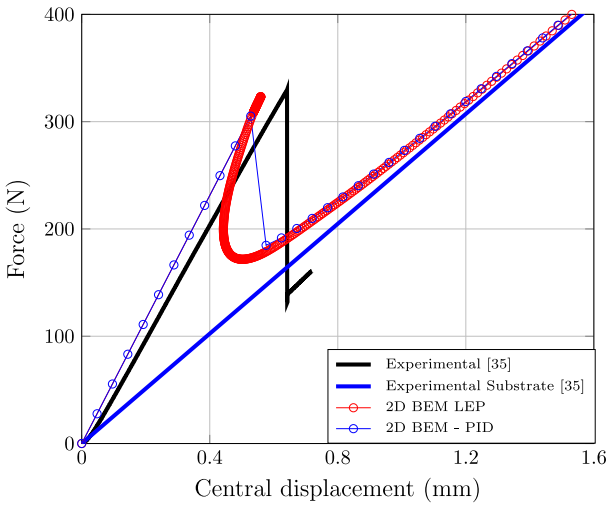

Fig. 27. Force–displacement results for asymmetric debonding: $h_s = 1.62$ mm.

of the adhesive-interface failure [50]. In such cases, the use of LEP is particularly practical as it involves a series of purely elastic simulations, which presents a significant advantage from an engineering perspective. Therefore, the combined BEM approach improves both computational efficiency and physical insight, making it especially suitable for adhesive bonding problems, where stress gradients are high.

7. Conclusion

This study employed the coupled criterion (CC) and a weak interface multizone boundary element method (BEM) to determine the critical stress and fracture toughness of the interface in three-point bending tests (3PBTs). The intrinsic mixed mode traction-separation model was then adopted to simulate the structural response using the obtained interface properties in the local interfacial cohesive stiffness matrices. Both symmetric and asymmetric debonding scenarios were analyzed for two substrate-adhesive systems, with the accuracy of the structural response predictions confirming the validity of the determined interface properties.

The adopted quantitative methodology with BEM models allows the quantification of the properties of the bonding adhesive interface and facilitates the analysis of adhesive debonding with fewer degrees of freedom. This approach retains the well-known advantages of BEM, such as precision in stress concentration problems and ease of model generation. Furthermore, the results of the stress distribution are consistent with analytical solutions, the macro-element method, and 3D FEM, further validating the methodology. The findings indicate that symmetric failure propagation using the proposed intrinsic mixed-mode traction-separation model significantly impacts the crack length - displacement curve, suggesting that future studies are needed to better understand the phenomenon. It is important to emphasize that the proposed model is evaluated primarily based on its ability to accurately predict key structural parameters such as peak load, crack initiation, and the overall failure path, factors that are most critical in the context of structural integrity and design. From this perspective, the model

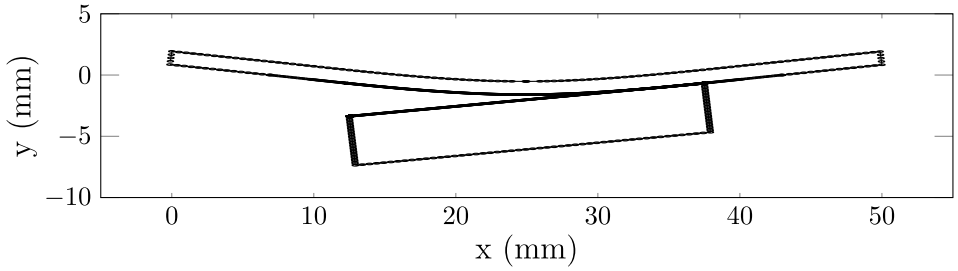

Fig. 28. C_n configuration for asymmetric debonding: $h_s = 1.08$ mm.

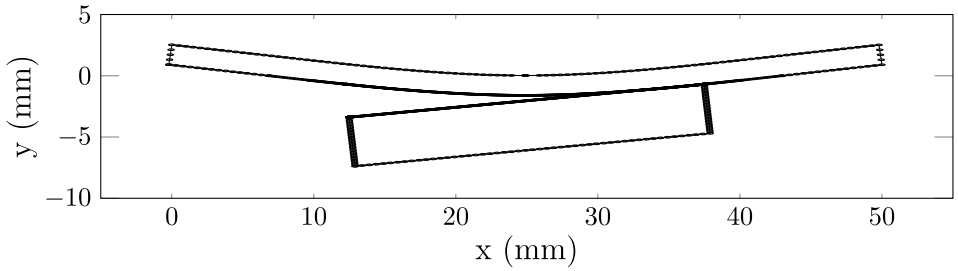

Fig. 29. C_n configuration for asymmetric debonding: $h_s = 1.62$ mm.

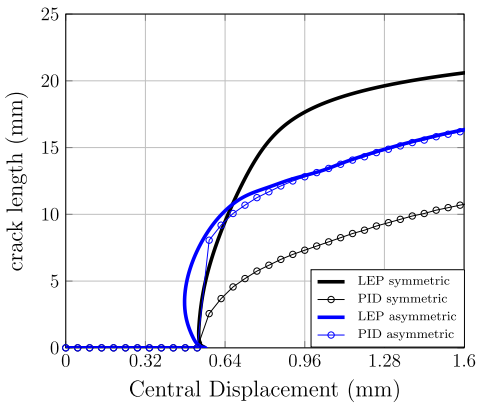

Fig. 30. Crack length-displacement results: $h_s = 1.08$ mm.

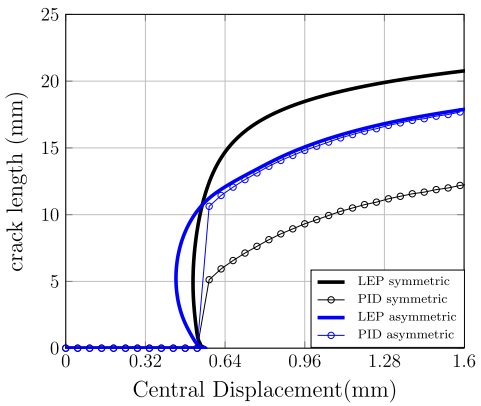

Fig. 31. Crack length-displacement results: $h_s = 1.62$ mm.

demonstrates reliable predictive performance and is considered valid for its intended application. Nevertheless, we acknowledge its current limitations in capturing the full complexity of the post-peak behavior. To address this, especially in the context of progressive damage analysis, ongoing developments include the implementation of nonlinear solvers of arch length and an enhanced traction–separation law incorporating mode-dependent fracture mechanisms. These improvements aim to refine the accuracy of the model in the post-peak regime and broaden its applicability to more complex failure scenarios.

CRediT authorship contribution statement

Sérgio Gustavo Ferreira Cordeiro: Writing – review & editing, Writing – original draft, Validation, Software, Methodology, Investigation, Formal analysis, Conceptualization. **Thiago V. Birro:** Writing – review & editing, Writing – original draft, Validation, Methodology, Conceptualization. **René Quispe Rodriguez:** Supervision, Software, Investigation, Conceptualization. **Eder Lima de Albuquerque:** Supervision, Resources, Investigation. **Lucas Silveira Campos:** Writing – original draft, Investigation, Conceptualization. **Jairo Francisco Useche Vivero:** Supervision. **Éric Paroissien:** Validation, Supervision, Methodology, Conceptualization. **Maëlenn Aufray:** Validation, Supervision, Conceptualization. **Frédéric Lachaud:** Validation, Supervision, Conceptualization.

Declaration of competing interest

The authors declare that they have no known competing financial interests or personal relationships that could have appeared to influence the work reported in this paper.

Acknowledgments

The authors gratefully acknowledge the Occitanie Region and the Université Fédérale de Toulouse Midi-Pyrénées / ISAE-SUPAERO for their financial support. Additionally, T. V. Birro would like to express sincere thanks to Sébastien Schwartz (ISAE-SUPAERO) for the helpful discussions regarding “normalized curves”. This work was carried out within the framework of the scientific network TACCOS (Toulouse Adhésion Cohésion Collage Structural): https://personnel.isae-supaero.fr/eric-paroissien/taccos-557.html, http://maelenn.aufray.free.fr/taccos.php.

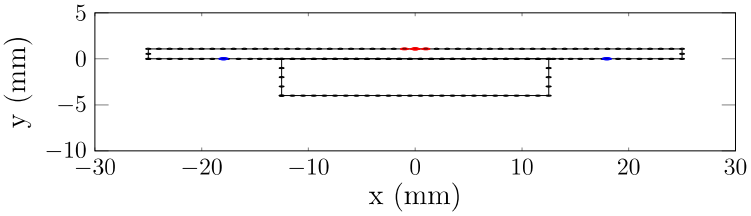

Fig. A.1. Mesh 0 adopted for the substrate-adhesive system $h_s = 1.08$ mm.

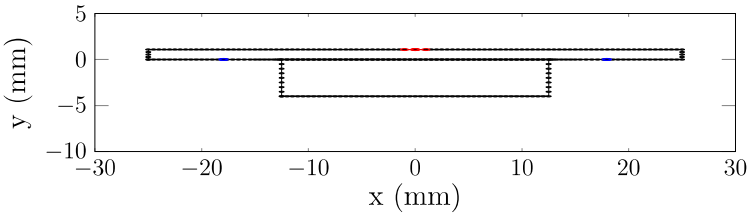

Fig. A.2. Mesh 1 adopted for the substrate-adhesive system $h_s = 1.08$ mm.

Appendix. Mesh convergence for the 2D BEM model

A mesh convergence study is presented to validate the 2D BEM models used in the analysis reported in Section 6. Three meshes were used to evaluate the peel and shear stresses at the interface: two coarse meshes and the fine mesh described in Section 6.1. The first coarse mesh, Mesh 0, consists of 171 linear elements, including 50 weak interface elements, 25 on each side. The element length is approximately 1.0 mm throughout the boundary. The second coarse mesh, Mesh 1, consists of 332 linear elements, including 100 weak interface elements, 50 on each side. The element length is approximately 0.5 mm throughout the boundary. Figs. A.1 and A.2 illustrate, respectively, the meshes Mesh 0 and Mesh 1 adopted for the substrate-adhesive system $h_s = 1.08$ mm.

On the other hand, the fine mesh, Mesh 2, used in Sections 6.1–6.3, is composed of 1486 elements of linear approximation, which include 1152 weak interface elements, 576 on each side. The initial 0.125 mm on both the left and right sides of the adhesive-substrate interface are discretized using a very fine mesh of 180 elements (720 elements/mm) to accurately capture the crack initiation according to the coupled criterion (CC).

The remaining 24.75 mm are discretized with 396 elements (16 elements/mm). Gradual refinement is also adopted in regions near the corner at the beginning of the adhesive-substrate interface. The boundary conditions are the same as those discussed in Section 6.1.

Figs. A.3–A.6 present the peel and shear stresses along the undamaged interface for the substrate-adhesive systems with $h_s = 1.08$ mm and $h_s = 1.62$ mm, obtained with the three meshes.

It is possible to observe from the results of the peel and shear stresses that the second coarse mesh, Mesh 1, is sufficient to accurately reproduce the elastic response of the test. However, the Mesh 2 was chosen for the analysis in Section 6 due to the requirements for the CC inverse analysis.

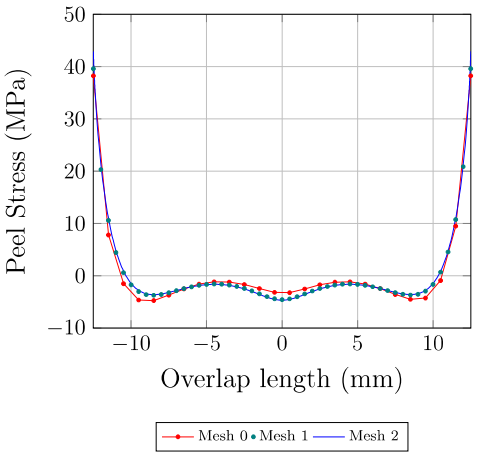

Fig. A.3. Mesh convergence: Peel Stress over the undamaged interface: $h_s = 1.08$ mm.

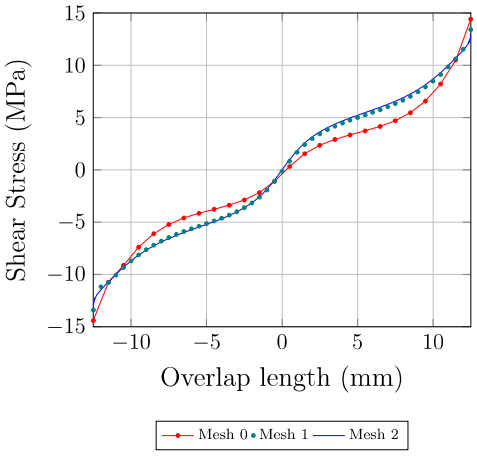

Fig. A.4. Mesh convergence: Shear stress over the undamaged interface: $h_s = 1.08$ mm.

Data availability

No data was used for the research described in the article.

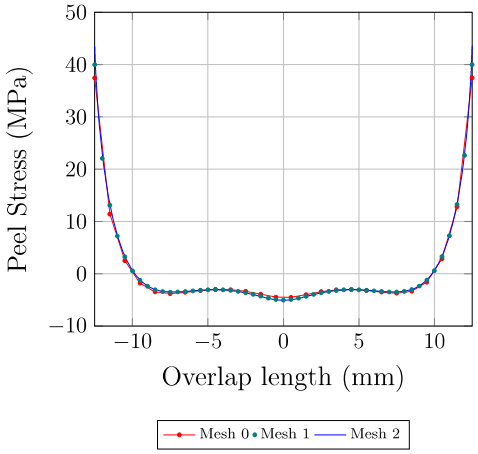

Fig. A.5. Mesh convergence: Peel Stress over the undamaged interface: h_s = 1.62 mm.

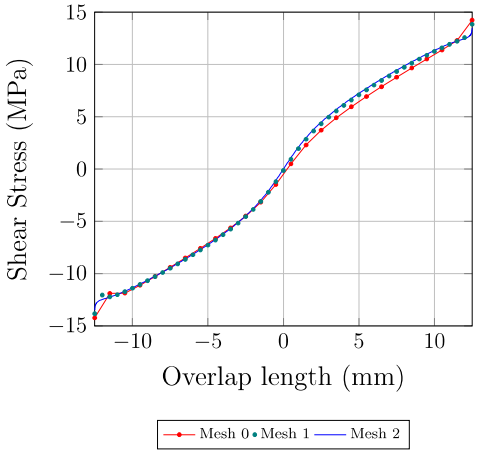

Fig. A.6. Mesh convergence: Shear stress over the undamaged interface: h_s = 1.62 mm.

References

[1] da Silva L, Öchsner A, Adams R. Handbook of adhesion technology. vol. 1, Springer Berlin Heidelberg; 2011.

[2] Rodríguez R, de Paiva W, Sollero P, Rodrigues E. Failure criteria for adhesively bonded joints. Int J Adhes Adhes 2012;37:26–36.

[3] da Silva L, Adams R. Techniques to reduce the peel stresses in adhesive joints with composites. Int J Adhes Adhes 2007;27:227–35.

[4] Duong C. A general approach to fracture analysis of tapered bonded joints and doublers. Eng Fract Mech 2012;96:355–79.

[5] Kinloch A. Adhesion and adhesives: Science and technology. Springer Netherlands; 1987.

[6] Mittal K. Adhesion measurement of thin films, thick films and bulk coating. ASTM International; 1978.

[7] Cornetti P, Mantič V, Carpinteri A. Finite fracture mechanics at elastic interfaces. Int J Solids Struct 2012;49:1022–32.

[8] Williams M. The stresses around a fault or crack in dissimilar media. Bull Seismol Soc Am 1959;49:199–204.

[9] Rice J. Elastic Fracture Mechanics Concepts for Interfacial Cracks. J Appl Mech 1988;55:98–103.

[10] Koguchi H, Yokoyama K, Luangarpa C. Variation of stress intensity factor along a small interface crack front in singular stress fields. Int J Solids Struct 2015;71:156–68.

[11] Távara L, Mantic V, Graciani E, París F. BEM analysis of crack onset and propagation along fiber–matrix interface under transverse tension using a linear elastic–brittle interface model. Eng Anal Bound Elem 2011;35:207–22.

[12] Birro T, Paroissien E, Aufray M, Lachaud F. Analytical solution for the interfacial stress and energy release rate at failure initiation of the three-point bending test (ISO 14679:1997). J Adhes Sci Technol 2024;1–44.

[13] Cornetti P, Pugno N, Carpinteri A, Taylor D. Finite fracture mechanics: a coupled stress and energy failure criterion. Eng Fract Mech 2006;73:2021–33.

[14] Leguillon D. Strength or toughness? A criterion for crack onset at a notch. Eur J Mech A Solids 2002;21:61–72.

[15] Martin E, Vandellos T, Leguillon D, Carrère N. Initiation of edge debonding: coupled criterion versus cohesive zone model. Int J Fract 2016;199:157–68.

[16] Weissgraeber P, Becker W. Finite fracture mechanics model for mixed mode fracture in adhesive joints. Int J Solids Struct 2013;50:2383–94.

[17] Muñoz-Reja M, Távara L, Mantič V, Cornetti P. A numerical implementation of the coupled criterion of finite fracture mechanics for elastic interfaces. Theor Appl Fract Mech 2020;108:102607.

[18] Mendoza-Navarro L, Diaz-Diaz A, Castañeda-Balderas R, Stéphane H, Noret R. Interfacial failure in adhesive joints: Experiments and predictions. Int J Adhes Adhes 2013;44:36–47.

[19] Leguillon D. An attempt to extend the 2D coupled criterion for crack nucleation in brittle materials to the 3D case. Theor Appl Fract Mech 2014;74:7–17.

[20] Barenblatt G. The formation of equilibrium cracks during brittle fracture. General ideas and hypotheses. Axially-symmetric cracks. J Appl Math Mech 1959;23:622–36.

[21] Tvergaard V, Hutchinson J. Toughness of an interface along a thin ductile layer joining elastic solids. Philos Mag A 1994;70:641–56.

[22] Wang Z, Xian G, Yue Q. Finite element modeling of debonding failure in CFRP-strengthened steel beam using a ductile adhesive. Compos Struct 2023;311:116818.

[23] Xu Y, Guo Y, Liang L, Liu Y, Wang X. A unified cohesive zone model for simulating adhesive failure of composite structures and its parameter identification. Compos Struct 2017;182:555–65.

[24] Gheibi M, Shojaeefard M, Googarchin H, Zaeri A. A generalized- park-Paulinho-roesler cohesive zone model to simulate moderate ductile adhesive joints. Int J Adhes Adhes 2023;126:103489.

[25] Vable M, JaiHind R. Boundary element analysis of adhesively bonded joints. Int J Adhes Adhes 2006;26(3):133–44.

[26] Muñoz-Reja M, Távara L, Mantič V, Cornetti P. Crack onset and propagation at fibre–matrix elastic interfaces under biaxial loading using finite fracture mechanics. Compos Part A: Appl Sci Manuf 2016;82:267–78.

[27] Cordeiro S, Daumas G, Monteiro F. A general DBEM for mixed-mode cohesive crack problems. Theor Appl Fract Mech 2024;130:104249.

[28] Tin-Loi F, Li H. Numerical simulations of quasibrittle fracture processes using the discrete cohesive crack model. Int J Mech Sci 2000;42:367–79.

[29] Vodička R. A quasi-static interface damage model with cohesive cracks: SQP–SGBEM implementation. Eng Anal Bound Elem 2016;62:123–40.

[30] Kormaníková E, Kšiňan F, Vodička R. Computational and experimental approaches for mode I delamination problems. Int J Solids Struct 2024;300:112926.

[31] Vodička R. A new quasi-static delamination model with rate-dependence in interface damage and its operation under cyclic loading. Int J Solids Struct 2021;224:111035.

[32] Cordeiro S, Teixeira G, Daumas G, Monteiro F. Numerical investigations in non-watertight models based on a surface-independent discretization boundary element method. Lat Am J Solids Struct 2023;20:e499.

[33] Roche A, Behme Jr A, Solomon J. A three-point flexure test configuration for improved sensitivity to metal/ adhesive interfacial phenomena. Int J Adhes Adhes 1982;2:249–54.

[34] Sauvage J, Aufray M, Jeandrau J, Chalandon P, Poquillon D, Nardin N. Using the 3-point bending method to study failure initiation in epoxide-aluminum joints. Int J Adhes Adhes 2017;75:181–9.

[35] Birro T, Paroissien E, Aufray M, Lachaud F. A methodology based on the coupled criterion for the assessment of adhesive-to-adherend interface crack initiation. Int J Adhes Adhes 2020;102:102664.

[36] ISO. Adhesives – Measurement of adhesion characteristics by a three-point bending method Norme. iso 14 679-1997, 1997.

[37] Devos P, Baziard Y, Rives B, Michelin P. Adherence evaluation of paint coatings using a three-point flexure test and acoustic emission. J Appl Polym Sci 2001;81:1848–57.

[38] Golaz B, Michaud V, Lavanchy S, M˚anson J. Design and durability of titanium adhesive joints for marine applications. Int J Adhes Adhes 2013;45:150–7.

[39] Weissgraeber P, Hell S, Becker W. Crack nucleation in negative geometries. Eng Fract Mech 2016;168:93–104.

[40] Doitrand A, Estevez R, Leguillon D. Comparison between cohesive zone and coupled criterion modeling of crack initiation in rhombus hole specimens under quasi-static compression. Theor Appl Fract Mech 2019;99:51–9.

[41] Griffith A. The phenomena of rupture and flow in solids. Trans R Soc A 1921;221:163–98.

[42] Martin E, Leguillon D. Energetic conditions for interfacial failure in the vicinity of a matrix crack in brittle matrix composites. Int J Solids Struct 2004;41:6937–48.

[43] Irwin G, Kies J. Critical energy release rate analysis of fracture strength. Weld J Res Suppl 1954;33:193–8.

[44] Park K, Paulino G. Cohesive zone models: a critical review of traction-separation relationships across fracture surfaces. Appl Mech Rev 2011;64:060802.
[45] Alfano G, Crisfield M. Finite element interface models for the delamination analysis of laminated composites: mechanical and computational issues. Internat J Numer Methods Engrg 2001;50:1701–36.
[46] Portela A, Aliabadi M, Rooke D. The dual boundary element method: Effective implementation for crack problems. Internat J Numer Methods Engrg 1992;33:1269–87.
[47] Blandford G, Ingraffea A, Liggett J. Two-dimensional stress intensity factor computations using the boundary element method. Internat J Numer Methods Engrg 1981;17:387–404.
[48] Aliabadi MH. The boundary element method, volume 2: applications in solids and structures. vol. 2, John Wiley & Sons; 2002.
[49] Doitrand A, Estevez R, Thibault M, Leplay P. Fracture and cohesive parameter identification of refractories by digital image correlation up to 1200° c. Exp Mech 2020;60(5):577–90.
[50] Birro TV, Aufray M, Paroissien E, Lachaud F. Assessment of interface failure behaviour for brittle adhesive using the three-point bending test. Int J Adhes Adhes 2021;110:102891.
[51] Muñoz-Reja M, Távara L, Mantič V. Symmetrical or non-symmetrical debonds at fiber–matrix interfaces: A study by BEM and finite fracture mechanics on elastic interfaces. J Multiscale Model 2017;08(03n04):1740008.
[52] Birro T. Prediction of adhesive failure of metallic bonded joints (Ph.D. thesis), Université de Toulouse; 2021, Université de Toulouse.
[53] Acary V, Monerie Y. Nonsmooth fracture dynamics using a cohesive zone approach. Research Report RR-6032, INRIA; 2006, p. 56.